

Licence

Please cite as:

Regnier J. et al. (2016). International benchmark on numerical simulations for 1D, nonlinear site response (PRENOLIN): verification phase based on canonical cases.

Bulletin of the Seismological Society of America, 106(5): 2112-2135

<https://doi.org/10.1785/0120150284>

1 International benchmark on numerical simulations for 1D,
2 non-linear site response (PRENOLIN): verification phase
3 based on canonical cases

- 4 Julie Régnier¹
- 5 Luis-Fabian Bonilla IFSTTAR, Paris, France
- 6 Pierre-Yves Bard IFSTTAR/ISterre, Paris-Grenoble, France
- 7 Etienne Bertrand, CEREMA, Nice, France
- 8 Fabrice Hollender, CEA, Cadarache, France
- 9 Hiroshi Kawase, DPRI, Kyoto, Japan
- 10 Deborah Sicilia, EDF, Aix-en-provence, France
- 11 Angelo Amorosi, Sapienza University of Rome, Italy
- 12 Dominic Assimaki, Caltech, Pasadena, US
- 13 Daniela Boldini, University of Bologna, Italy
- 14 Long Chen, Univ. Washington, Seattle, US
- 15 Anna Chiaradonna, Univ. Napoli, Italy
- 16 Florent DeMartin, BRGM, Orléans, France
- 17 Marco Ebrille, Politecnico di Torino, Torino, Italy

¹ *Julie.regnier@cerema.fr, CEREMA, DTer Méditerranée, 56 Bd de Stalingrad*

06300 Nice

- 18 Gaetano Falcone, Politecnico of Bari, Italy
- 19 Evelyne Foerster, CEA, Saclay, France
- 20 Sebastiano Foti, Politecnico di Torino, Torino, Italy
- 21 George Gazetas, NTUA, Athena, Greece
- 22 Céline Gélis, IRSN, Fontenay-aux-roses, France
- 23 Alborz Ghofrani, Univ. Washington, Seattle, US
- 24 Jim Gingery, UCSD, San Diego, US
- 25 Nathalie Glinsky, CEREMA, Nice, France
- 26 Joseph Harmon, Univ. Illinois at Urbana-Champaign, US
- 27 Youssef Hashash, Univ. Illinois at Urbana-Champaign, US
- 28 Susumu Iai, DPRI, Kyoto, Japan
- 29 Boris Jeremić, UCD, Davis, US
- 30 Steve Kramer, Univ. of Washington, US
- 31 Stavroula Kontoe, Imperial College, London, England
- 32 Jozef Kristek, CUB, Bratislava, Slovakia
- 33 Giuseppe Lanzo, Univ. Rome, Rome, Italy
- 34 Annamaria di Lernia, Politecnico of Bari, Italy
- 35 Fernando Lopez-Caballero, Centrale Supélec Paris, France
- 36 Marianne Marot, CEREMA, Nice, France
- 37 Graeme McAllister, UBC, Vancouver, Canada

- 38 E.Diego Mercerat, CEREMA, Nice, France
- 39 Peter Moczo, CUB, Bratislava, Slovakia
- 40 Silvana Montoya-Noguera, Centrale Supélec, France
- 41 Michael Musgrove, Univ. Illinois, US
- 42 Alex Nieto-Ferro, EDF, Clamart, France,
- 43 Alessandro Pagliaroli, CNR-IGAG, Rome, Italy
- 44 Federico Pisanò, Delft University of technology, Delft, The Netherlands
- 45 Aneta Richterova, CUB, Bratislava, Slovakia
- 46 Suwal Sajana, Univ. Rome, Rome, Italy
- 47 Maria Paola Santisi d'Avila, UNS, Nice, France
- 48 Jian Shi, Caltech, Pasadena, US
- 49 Francesco Silvestri, Univ. Napoli, Napoli, Italy
- 50 Giuseppe Tropeano, Univ. Cagliari, Cagliari, Italy.
- 51 Luca Verrucci, Univ. Rome, Rome, Italy
- 52 Kohei Watanabe, Shimizu Corporation, Tokyo, Japan.²
- 53

² The author's list involves first the seven organizers of the PRENOLIN project followed by the participants in an alphabetic order.

54 **Abstract**

55 PRENOLIN is an international benchmark presently underway to test multiple numerical
56 simulation codes capable of predicting non-linear seismic site response with various
57 constitutive models. One of the objectives of this project is the assessment of the uncertainties
58 associated with non-linear simulation of one-dimensional (1D) site effects. A first verification
59 phase (i.e. comparison between numerical codes on simple, idealistic cases) will be followed
60 by a validation phase, comparing the predictions of such numerical estimations with actual
61 strong motion recordings obtained at well-known sites. The benchmark presently involves 19
62 different prediction teams and 23 different non-linear computational codes.

63 We present here the main results of the verification phase dealing with simple cases. Three
64 different idealized soil profiles were tested over a wide range of shear strains with different
65 input motions and different boundary conditions at the sediment/bedrock interface. A first
66 iteration focusing on the elastic and visco-elastic cases proved to be useful to ensure a
67 common understanding and to identify numerical issues before pursuing the non-linear
68 modeling. Besides minor (but always possible...) mistakes in the implementation of input
69 parameters and output units, the initial discrepancies between the numerical results can be
70 attributed to (1) different understanding of the expression "input motion" in different
71 communities, and (2) different implementations of material damping and possible numerical
72 dispersion. The second round of computations thus allowed a convergence of all teams to the
73 Haskell-Thomson analytical solution in elastic and visco-elastic cases. For non-linear
74 computations we investigate the epistemic uncertainties related only to wave propagation
75 modeling using different non-linear constitutive models. Such epistemic uncertainties are
76 shown to increase with the strain level and to reach values around 0.2 (natural log scale) for a

77 5m/s² reference motion, which may be reduced by almost 50% when the various constitutive
78 models do use the same shear strength and damping implementation.

79

80 **Introduction**

81 Including site effects in seismic hazard assessments requires the consideration, at some stage,
82 of non-linear behavior of soils, which may greatly affect their dynamic responses to strong
83 motion and significantly modify their amplifications behavior compared to weak motion
84 (computed or measured). Even in areas of moderate seismicity, the hazard level at long to
85 very long return periods (i.e., several thousands to tens of thousands years) may be large
86 enough to generate significant strains in shallow, soft soil layers, which in turn leads to a
87 degradation of their mechanical properties such as hysteretic behavior with loss of shear
88 stiffness and increased energy dissipation (Bonilla et al., 2005; Iai et al., 1995; Ishibashi and
89 Zhang, 1993; Seed, 1969; Vucetic and Dobry, 1991; Yu et al., 1993; Zeghal et al., 1995).

90 Such dependence of the dynamic soil response on the level of seismic loading, conventionally
91 denoted as "non-linear effects" (Beresnev et al., 1995), involves rather complex mechanical
92 processes, which may be grouped roughly in two main classes. The first is the degradation of
93 the mechanical properties of the material, which is often characterized by a decrease in the
94 shear modulus coupled with an increase in energy dissipation; while the second is related to
95 pore pressure changes in water-saturated granular soils, linked with volumetric changes of the
96 soil skeleton under shear stress, and may generate liquefaction in loose sandy soils. Our
97 interest here focused on the first type of non-linearity, without any consideration of pore
98 water pressure generation or liquefaction.

99 The first type of non-linear effect (i.e. without liquefaction) was identified by geotechnical
100 earthquake engineering studies following the 1967 Caracas earthquake, and was later
101 confirmed both by laboratory tests and recordings obtained on "vertical arrays" with two or
102 more accelerometric sensors at different depths within the same borehole. For instance, a

103 statistical analysis of the numerous recordings of the Japanese KiKnet network (Régnier et al.,
104 2013) concluded that, for Peak Ground Acceleration (PGA) levels exceeding 0.75 m/s^2 (a
105 rather moderate level) at an outcrop, there is a 40 % chance of observing a non-linear soil
106 response, leading to significant modifications with respect to the linear, low-strain response.
107 These changes generally imply a reduction of the response amplification of the signal's high-
108 frequency content and often a slight-to-significant increase of its low frequency content.
109 Therefore, linear soil response estimates cannot be considered as being systematically on the
110 safe side, and on the other hand, the high frequency reductions may significantly contribute to
111 the safety margins. As a consequence, the accuracy, robustness and reliability of non-linear
112 site effects prediction directly impacts the estimation of seismic hazard and associated risks,
113 especially at long return periods.

114 While a consensus has undoubtedly been reached on the existence of non-linear effects, their
115 quantification and modeling remains a challenge. Indeed, numerous techniques have been
116 proposed for the assessment of site effects in the linear domain using empirical and/or
117 modeling approaches on generic or site-specific basis. Conversely, empirical estimation of
118 non-linear site effects is more limited, especially in moderate seismicity areas where the on-
119 site instrumental approach can only be a long (to very long)-term investment. Aside from a
120 generic approach based on existing recordings (Derras et al., 2012; Sandikkaya et al., 2013),
121 the only presently possible way for site-specific estimates is thus numerical simulation.
122 Obviously, such analysis must be preceded by a precise geotechnical and geophysical
123 characterization of the underground structure, and the choice of a suitable non-linear
124 constitutive model.

125 Given the complexity of non-linear behavior of soils, many constitutive models and codes
126 have been developed for such simulations. When the deformation remains moderate (i.e.,
127 smaller than about 0.1-0.3 %), the so-called "equivalent linear model", which is a linear

128 approach with an iterative adjustment of visco-elastic properties (shear modulus and
129 damping) to the local strain level, is often used and accepted in practice. However, when the
130 strain level exceeds these values (i.e., above 0.2-0.5 %), which can occur in very soft soils
131 and/or with very strong input motions, a complete non-linear modeling, with an appropriate
132 constitutive law fed by the correct soil parameters is required. These models fall into two
133 categories: relatively simple constitutive laws with few parameters, that cannot reproduce a
134 wide range of loading/unloading paths; and more complex models with many parameters
135 (sometimes exceeding 10), which can succeed in describing all possible behaviors, but with
136 parameters that can be difficult to determine or calibrate.

137 The ability to accurately predict non-linear site responses has indeed already been the subject
138 of two recent comparative tests. It was one of the targets of the pioneering blind tests initiated
139 in the late 80's/early 90's, on 2 sites of Ashigara Valley (Japan) and Turkey Flat (California);
140 however, those sites lacked strong motion records until the 2004 Parkfield earthquake during
141 which the Turkey Flat site experienced a 0.3 g motion. Since the soils were fairly stiff, the
142 nonlinearity was not very strong. A new benchmarking of 1D non-linear codes was thus
143 carried out in the last decade, based on the Turkey Flat site and a few other sites with vertical
144 array data (La Cienega, California; the KGWH02 KiK-net site in Japan, and Lotung in
145 Taiwan). Its main findings, reported by Kwok et al. (2008) and in (Stewart and Kwok, 2009)
146 emphasized the key importance of the way these codes are used and of the required in-situ
147 measurements. Significant differences between records and predictions have been postulated
148 as being due to an incorrect velocity profile (although it was derived from redundant borehole
149 measurements), a non-1D soil geometry (non-horizontal layers), and imperfections /
150 deficiencies in the constitutive models, which were unable to represent the actual curves for
151 stiffness reduction and damping increase. Another test was undertaken on the Euroseis
152 European test site (Mygdonian graben near Thessaloniki, Greece) as part of the

153 Cashima/E2VP project, which included two separate exercises on two-dimensional (2D) non-
154 linear numerical simulation codes and three-dimensional (3D), linear simulation codes. The 2D
155 non-linear (NL) benchmark proved inconclusive, as major differences were found between
156 the few considered codes, with multiple possible causes (2D numerical scheme, damping
157 implementation, and NL constitutive laws (see Foerster et al., 2015). Given the fact that the
158 codes used for these tests are routinely used in engineering practice for predictions of non-
159 linear site responses, especially for moderate seismicity countries lacking strong motion
160 recordings, there is a clear need to conduct further tests in better controlled conditions, in
161 particular with in situ and laboratory measurements for an optimal tuning of the non-linear
162 parameters used in each code.

163 For this reason, the PRENOLIN project considers only 1D soil columns to test the non-linear
164 codes in the simplest possible, though realistic, geometries. It is organized in two phases: (1)
165 a verification phase aiming at a cross-code comparison on very simple (and "idealistic") 1D
166 soil columns with prescribed linear and non-linear parameters; (2) a validation phase for
167 comparison between numerical predictions and actual observations, for sites as close as
168 possible to a 1D geometry (horizontal stratification), without liquefaction evidence and with
169 already available sets of downhole and surface recordings for weak to very strong motions
170 and later complemented by careful in-situ and laboratory measurements designed as close as
171 possible to the participants requirements. The sites were selected within the Japanese KiK-net
172 and PARI (Port and Airport Research Institute) accelerometric networks.

173 The purpose of this article is to present and discuss the results of the verification phase, with a
174 special focus on the epistemic uncertainties associated with the constitutive laws and
175 numerical schemes of the simulation codes. The first section describes the 3 idealized soil
176 columns and the requested computations, considering different boundary conditions (rigid /
177 elastic base, associated respectively with within / outcropping reference motion). The next

178 section lists the numerous teams that volunteered to participate in this exercise and the main
179 characteristics of their codes. The simulation results are then presented and compared, first in
180 the linear case (with and without attenuation), and then in the non-linear case for various input
181 signals and levels, with a discussion in each case on the amount and origins of uncertainty.

182 **The canonical cases**

183 The verification phase of this project aims at establishing the similarity between the computed
184 wave motions at the surface of a soil column affected by amplification using different
185 numerical codes, quantifying the amount of code-to-code differences and, as much as
186 possible, understanding them. The computed responses were compared with analytical
187 solutions when available. Figure 1 summarizes the calculations performed during the
188 verification phase, for the linear (elastic and visco-elastic), and non-linear cases. In the elastic
189 and visco-elastic cases, for which analytical results are available and provided that all
190 participants/users share a common understanding of the physical soil parameters to be used,
191 no differences (or minor) in the results are expected. These first calculations are needed in
192 order to ensure a proper predictability of the induced deformation (shear strain) for all soil
193 and seismic wavefield properties. On the other hand, for non-linear cases, discrepancies
194 between the different computations are expected: the goal is to identify their origins in
195 relation to the constitutive models and/or the numerical schemes (or other possible issues), to
196 quantify the associated epistemic uncertainty, and to reduce it to its minimum level as much
197 as possible.

198 The experiment was designed around three 1D canonical cases, chosen to represent simple
199 and idealistic soil conditions overlying stiff bedrock substrata:

- 200 1) Profile 1 (P1) is a shallow (20 m thick), homogeneous soil layer presenting a
201 significant velocity impedance ratio at rock, with amplification in the intermediate
202 frequency range [2-10 Hz].
- 203 2) Profile 2 (P2) is a thick (100 m) soil layer with S-wave velocity gradually increasing
204 with depth, overlying a very stiff bedrock, with a low fundamental frequency (below 1
205 Hz).
- 206 3) Profile 3 (P3) consists of two homogeneous layers with moderate velocity contrasts,
207 overlying a very stiff bedrock, with expected amplification effects in the intermediate
208 frequency range (2-10 Hz). The goal is to investigate non-linearity effects within both
209 layers, since significant strains can develop at or near each interface.

210 Various reference motions are considered for each profile, from very simple signals intended
211 to capture the basic physics of NL behavior (pulse like and cyclic, quasi-monochromatic
212 signals with increasing amplitude), to realistic accelerograms. For the later, two strong
213 motions were selected with very different spectral content (high and low frequency contents),
214 and scaled to three PGA levels, in order to generate a wide range of shear strain levels in the
215 soil column.

216 These reference motions were applied at the bedrock level, with two boundary conditions
217 representative of the actual case studies: in one case, the reference motion was considered to
218 mimic the outcropping motion at the surface of the underlying bedrock ("elastic" condition),
219 while in the other it was considered to mimic the "within" motion recorded by a virtual sensor
220 at the sediment-bedrock interface ("rigid" condition).

221 *Figure 1 : The three simple idealized profile cases studied here (P1-3), for the elastic and non-elastic*
222 *domains, and for a rigid and elastic soil-bedrock base, using a Ricker pulse and 3 accelerations of different*
223 *PGA and frequency contents.*

224 ***Soil properties***

225 The properties describing the (1D) linear and non-linear soil behavior for each profile include
226 elastic, visco-elastic and non-linear soil properties. They are displayed in Figure 1 and Figure
227 2, and summarized in Table 1.

228 The basic characteristics of soil profiles (i.e., thickness, density and seismic waves velocities)
229 were chosen in order to be representative of typical soil profiles. Values of P-waves velocity
230 (V_P) are derived from the profiles of S-waves velocity (V_S) shown in Figure 2, using assumed
231 values of Poisson ratio (0.4 for soil and 0.3 for bedrock). Profiles P1 and P3 exhibit constant
232 seismic velocities in each layer, while P2 includes a velocity gradient with a regular increase
233 from $V_S = 150$ m/s at the surface to $V_S = 500$ m/s at the soil-bedrock interface, according to
234 the equation:

$$235 \quad V_S(z) = V_{S1} + \left(\frac{V_{S2} - V_{S1}}{Z_2 - Z_1} (z - Z_1) \right)^\alpha$$

236 ***Eq 1***

237 where $V_{S1} = 150$ m/s and $V_{S2} = 500$ m/s are the shear-wave velocities at depths $Z_1 = 0$ m and
238 $Z_2 = 100$ m, respectively, and $V_S(z)$ is the shear wave velocity at depth z ; α is taken equal to
239 0.25.

240

241 **Visco-elastic properties**

242 We only consider intrinsic material damping (Biot, 1956; Johnston et al., 1979; Leurer, 1997),
243 without any additional component from scattering. Intrinsic attenuation can be quantified by
244 the quality factor Q (more commonly used in seismology), or the damping ratio ξ (used in
245 engineering seismology). Here Q and ξ are the quality factor and the damping ratio of the S-

246 waves. They are linked by the formula $Q = 1/(2\xi)$, and can be determined by the loss of
247 energy over one wavelength. Pure elastic materials totally restore the seismic energy after
248 deformation, and should therefore have infinite Q values; as the numerical codes used here
249 require a finite value as input, the "elastic" case was computed with very high values of Q
250 (very low ξ) for both soil and bedrock ($Q = 5000$). For visco-elastic and non-linear (soft)
251 materials, the energy dissipation at low strain was constrained to vary according to V_s ,
252 through the classical – never appropriately justified by measurements - relationship $Q =$
253 $V_s/10$, or equivalently $\xi = 5/V_s$ (V_s in m/s) (Olsen et al., 2003).

254 **Non-linear soil properties**

255 The non-linear properties of each layer were characterized using classical $G/G_{\max}(\gamma)$ and $\xi(\gamma)$
256 curves, relating the decay of shear modulus (G) normalized by the elastic shear modulus
257 (G_{\max}) and increase of damping ξ with the shear strain γ . The $G/G_{\max}(\gamma)$ and $D(\gamma)$ curves were
258 constructed following a simple hyperbolic model based on the following equations:

$$259 \quad K_0 = (1 - \sin(\phi)) \cdot OCR^{\sin(\phi)}$$

260 **Eq 2**

$$261 \quad \sigma'_m = \sigma'_v (1 + 2K_0) / 3$$

262 **Eq 3**

$$263 \quad \tau_{\max} = \sigma'_m \sin(\phi)$$

264 **Eq 4**

$$265 \quad \gamma_{ref} = \tau_{\max} / G_{\max}$$

266 **Eq 5**

267 $G/G_{\max} = 1/(1 + \gamma/\gamma_{ref})$

268 **Eq 6**

269 $\xi = \xi_{\min} + (\xi_{\max} - \xi_{\min})(\gamma/\gamma_{ref})/(1 + \gamma/\gamma_{ref})$

270 **Eq 7**

271 where the control parameters are the friction angle $\Phi = 30^\circ$, the over-consolidation ratio OCR
272 = 1 and the gravitational acceleration $g = 9.81 \text{ m/s}^2$. Only cohesionless material was
273 considered here, so that the shear strength τ_{\max} is computed using the vertical stress and the
274 friction angle. Both, σ_m' and σ_v' are the effective mean and vertical stresses; γ is the shear
275 strain. The reference shear strain γ_{ref} corresponds to the strain for which $G = 0.5G_{\max}$ (in the
276 hyperbolic model as describe above it is given by Eq 5), K_0 is the coefficient of earth pressure
277 at rest, and ξ_{\min} and ξ_{\max} are the minimum damping values at very low strain (= intrinsic
278 material damping considered above for the visco-elastic behavior), and the maximum at very
279 high strain, respectively.

280 Only one $G/G_{\max}(\gamma)$ and $\xi(\gamma)$ curves were provided for P1, five for P2 (increasing for each 20
281 m depth interval), and two for P3 (one for each homogeneous layer). We assume a constant
282 strength per soil layer for all soil models. They are illustrated in Figure 2. For P1 and P2, they
283 are fitting a hyperbolic curve defined by the low strain shear modulus $G_{\max} = \rho V_s^2$ and the
284 shear strength τ_{\max} at the center of each layer or sublayer. For P3 the $G/G_{\max}(\gamma)$ and $\xi(\gamma)$
285 chosen models were very similar to one another using the previous hyperbolic model. For P3,
286 the set of Darendeli models (Darendeli, 2001) was used and adjusted to a simple hyperbolic
287 model as for P1 and P2; as Darendeli's models are defined only up to a maximum shear strain
288 of 1 %, the P3 curves were defined by multiplying the shear strength τ by factors 1.1 and 2 at
289 depths of 10 m and 35 m, respectively, and the final curves were then computed based on the
290 hyperbolic models associated to these values.

291 Some numerical codes include sophisticated constitutive models for NL soil behavior, which
292 require very specific additional parameters, which should be consistent with the $G/G_{\max}(\gamma)$
293 and $\xi(\gamma)$ curves supplied for the other codes. The definition of these additional parameters was
294 done individually by each team, with the following simple assumptions: the soil is
295 cohesionless (i.e. $c' = 0$ and Plasticity Index $PI = 0$), and the water table is located at 100m
296 depth, the soil particle size distribution is defined with $D_{10} = 0.2$ mm and $D_{50} = 0.35$ mm, and
297 a uniformity coefficient $= D_{60}/D_{10} = 1.8$.

298

299

TABLE 1

300

*Figure 2 : Vs profiles, G/G_{max} and damping curves for the 3 idealized profiles.***301 Reference rock motion**

302 In the first phase of the project, each participant was provided (i) a simple Ricker pulse input
 303 motion derived analytically, and (ii) two real acceleration time histories scaled to three
 304 different PGA levels (0.5, 1 and 5 m/s²) to observe the evolution from linear to non-linear soil
 305 behavior. The two accelerograms were selected to be representative of very different
 306 frequency contents, in order to analyze its influence in the non-linear computations. Each
 307 accelerogram was pre-processed in the same way as explained further below. The Fourier
 308 transform of the three normalized input motions are illustrated in Figure 3.

309 The pulse-like input motion

310 The Ricker pulse input motion corresponds to acceleration, velocity and displacement time-
 311 histories defined by equations (8) to (10). A central frequency of 4 Hz was chosen to produce
 312 sufficient energy at the fundamental frequency of each of the three profiles, while having a
 313 broad band energy in the main bandwidth of earthquake geotechnical engineering, i.e. 1 -10
 314 Hz.

$$315 \quad a(t) = [1 - 2(\pi f_c t)^2] \exp(-(\pi f_c t)^2)$$

316 **Eq 8**

$$317 \quad v(t) = t \exp(-(\pi f_c t)^2)$$

318 **Eq 9**

$$319 \quad d(t) = \frac{1}{-2(\pi f_c)^2} \exp(-(\pi f_c t)^2)$$

320 **Eq 10**

321 where f_c is the central frequency and $a(t)$, $v(t)$ and $d(t)$ are the acceleration, velocity and
322 displacement time histories, respectively. The acceleration time histories and the normalized
323 Fourier Transform spectra for the three input motions are illustrated in Figure 3.

324 **Real reference input motions**

325 To investigate the effect of frequency content on the computation of non-linear soil behavior,
326 we used two real input motions with different frequency contents recorded at rock outcrop
327 sites. One has a predominant frequency of 11.4 Hz, and the other of 4.8 Hz: they are labeled
328 hereafter HF and LF, respectively. The metadata of these two recordings are described in
329 Table 2 and their acceleration, velocity and displacement time histories are illustrated in
330 Figure 3. We can observe that the spectral shape are quite different, the main energy of the
331 signal for the LF motion lies between 0.5 to 10 Hz and for the HF motion between 5 to 20 Hz.
332 The duration of the HF event is about 80 s while it is shorter for the LF motion around 15 s.
333 In this work, we considered only the horizontal EW component of each recording.

334 **TABLE 2**

335 The velocity and displacement time histories of these two recordings were calculated from the
336 original raw acceleration data, following this procedure: (1) removal of the mean, (2) zero
337 padding of the signal by applying Boore's approach (Boore and Bommer, 2005) over a
338 specific time duration corresponding to 20 s before the first, and after the last, zero-crossing
339 of the original acceleration time series, (3) high-pass filtering of the signal, and (4) integrating
340 twice to obtain consistent velocity and displacement time histories.

341 *Figure 3: Normalized reference motion used for the verification phase of this project PRENOLIN.*

342

343 **Participants and tested numerical codes**

344 We compared 23 different numerical codes used by 21 participating teams, as listed in Table
345 3. As some teams use several codes, each computational case/team is annotated by a letter and
346 a number. Two or more teams used the same code, including Deepsoil (4 teams for the
347 verification and 5 for the validation), FLAC (2 teams) and OpenSees (3 teams). Others used
348 the same constitutive model, notably Iai's (1990) model (2 teams), Iwan's model (Ishihara,
349 1996; Iwan, 1967) (4 teams) and the Hujoux model (Aubry et al., 1982) (2 teams). The
350 participants teams were composed by people having different background and expertise
351 which can relevant for analyzing the site response variability. Firstly, two disciplines are
352 represented in this benchmark, seismology and geotechnical earthquake engineering and
353 secondly, the participants are either developers or users.

354 We identified three different, non-exclusive code groups, according to three main
355 characteristics: (1) the type of numerical scheme, (2) the way to implement the attenuation,
356 either in the low strain range or in the large strain range, and (3) the type of non-linear
357 constitutive models. Each of these three groups is detailed in the next sections.

358

359 **TABLE 3**

360 ***The numerical scheme***

361 The 20 codes that solve the problem in time domain are split in two main categories: two
362 types of spatial approximations are considered:

363 (a) The Finite Element Method (FEM) is by far the most common, used by 18 teams and
364 implemented in three different ways:

365 i) Standard method (ST.FEM), used by 12 teams: B-0, D-0, H-0, L-1, M-1, N-0, R-
366 0, S-0, T-0, U-0, W-0 and Z-1.

367 ii) Spectral method (SP.FEM), used by 1 team: Q-0

368 iii) Discontinuous Galerkin method (DG.FEM), used by 1 team: Y-0.

369 (b) The Finite Difference Method (FDM) is used by 10 teams: A-0, C-0, E-0, F-0, G-0, J-
370 0, K-0, L-2, M-0 and M-2;

371 The last remaining teams (J-1, T-1 and Z-0) consider the problem in the frequency domain
372 and use a linear equivalent method involving linear, visco-elastic material with several
373 iterations to tune the visco-elastic properties in each layer to the shear strain and modulus
374 reduction and damping curves (Schnabel et al., 1972).

375 ***Implementation of attenuation***

376 **Low strain attenuation:** At low strain levels (less than 10^{-4} - 10^{-2} %), elasto-plastic
377 constitutive models and most of the non-linear models have damping values close to zero,
378 which is physically unrealistic, since all soils and rocks exhibit a hysteretic behavior in the
379 stress-strain plane even for weak deformations, indicating dissipation of energy.

380 In the frequency domain, implementation of a prescribed attenuation factor is relatively
381 straightforward. In theory, fulfillment of the causality principle leads to a (slight) frequency
382 dependence of the shear wave velocity, which should be specified (together with the damping

383 value) at a specific frequency f_0 (Aki and Richards, 2002) . However, this is not implemented
384 in all codes: some consider a truly frequency-independent attenuation with a defined reference
385 frequency for the velocity, while some dropped the causality principle and have frequency
386 independent velocities.

387 In the time domain, attenuation can be approximated by implementation of a set of relaxation
388 functions using rheological models such as the generalized Maxwell model (Blanch et al.,
389 1995; Day and Bradley, 2001; Day and Minster, 1984, 1984; Graves and Day, 2003) or
390 modeled by a Rayleigh damping formulation. Both methods present pros and cons. The usage
391 of rheological models to approximate attenuation is physical; however, adds memory
392 constraints to the computations. The greater the number of relaxation functions used, the
393 better the attenuation factor will be approximated (although one should not use too many (see
394 for example Peyrusse et al., 2014). On the contrary, the Rayleigh damping method is much
395 easier to be implemented numerically; nevertheless, the parameters are not easily determined,
396 and automatically involve a significant frequency dependence of Q . For low attenuation
397 (below a damping ratio of 20%) it has been shown that Rayleigh damping and the generalized
398 Maxwell model become equivalent (Semblat, 1997).

399 For the entire set of codes tested here, four kinds of attenuation implementations were used:

400 (1) Frequency-independent attenuation (frIA): Some model considered frequency
401 independent attenuation instead of the use of the frequency dependent Rayleigh
402 Damping/attenuation in the time domain analysis. Models A-0, E-0, K-0, Q-0, T-1 and
403 Z-0 use series of Maxwell/Zener elements (Blanch et al., 1995; Day and Bradley,
404 2001; Day and Minster, 1984, 1984; Graves and Day, 2003), which imply an almost
405 constant attenuation over a specific, broad enough frequency range. Models F-0, J-0
406 and M-2 used the frequency independent attenuation as proposed in (Phillips and
407 Hashash, 2009a).

408 (2) Frequency-dependent attenuation (frDA), such as the Rayleigh damping (simplified or
409 full). It was used by 10 teams: B-0, G-0, H-0, L-1, M-0, M-1, R-0, S-0, T-0, W-0, Y-0
410 and Z-1.

411 (3) Low strain frequency independent hysteretic damping (LSHD). It was used by 4
412 teams: C-0, N-0, D-0 and R-0.

413 (4) Numerical damping (ND). 3 teams (U-0, N-0 and D-0) use variant of the Newmark
414 integration scheme to simulate attenuation effects with purely numerical damping
415 tools, while another team (L-1) used it to filter out numerical noise (NDfilt).

416

417 **High strain attenuation:** High strain attenuation can be computed directly from the
418 hysteretic behavior of the soil subjected to strong ground motion (loading / unloading cycles).
419 However, it was demonstrated it is difficult to reproduce simultaneously the specified
420 decrease of G/G_{\max} with increasing shear strain, and the increasing of damping. For this
421 reason, a few teams (A-0, B-0, E-0 and T-0) chose to use a “damping control” (which implies
422 a modification of the "Masing rules, and is thus labeled as ‘no-Masing rules’): it is based on a
423 mapping that converts a hysteresis loop in such a way that it will satisfy the hysteretic
424 damping at the current strain level (IAI et al., 1992). Other teams (J-0) used the method as
425 proposed in Phillips and Hashash (2009a) which modifies the unload and reload rules of the
426 extended Masing rules.

427 *Non-linear constitutive models*

428 In geotechnical earthquake engineering, non-linear soil behavior is a well-established concept.
429 In laboratory experiments, such as cyclic tri-axial tests, the non-linear soil behavior is
430 expressed by hysteresis loops in axial stress-strain plots, which can be linked to shear stress-
431 strain plots. The soil response under cyclic loading (representing seismic loading) depends on

432 the properties of the cyclic loading (e.g. time history, peak amplitude) and on the soil
433 properties (e.g. strength, relative density).

434 In non-linear models, the true hysteresis soil behavior is simulated by the use of constitutive
435 models which mimic the experimental hysteresis curves, or the shear modulus decay
436 ($G/G_{\max}(\gamma)$) and attenuation ($\xi(\gamma)$) curves.

437 According to information gathered from each participant, the codes tested here are
438 implemented with various non-linear models, including:

439 \Rightarrow Iai model (Iai et al., 2011; Iai and Ozutsumi, 2005): B-0, E-0,

440 \Rightarrow MKZ modified hyperbolic model (Matasovic and vucetic, 1995, 1993): A-0

441 \Rightarrow Cundall's model (Cundall, 2006): M-0

442 \Rightarrow Iwan's model (Ishihara, 1996; Iwan, 1967): K-0, Q-0, U-0, Y-0

443 \Rightarrow Logarithmic function model (Puzrin and Shiran, 2000) : L-1

444 \Rightarrow Modified Hujieux model (Aubry et al., 1982): D-0, N-0, S-0

445 \Rightarrow Multiyield model (Elgamal et al., 2003; Yang et al., 2003): H-0

446 \Rightarrow Extended Hyperbolic model (Phillips and Hashash, 2009b) : F-0, H-0, J-0, M-2, T-0

447 \Rightarrow HSsmall (Isotropic hardening elasto-plastic soil model) (Schanz et al., 1999): Z-1

448 \Rightarrow Pisanò 3D Elastic-plastic model (Pisanò and Jeremić, 2014): R-0;

449 \Rightarrow BWGG: Extended Bouc Wen model (Gerolymos and Gazetas, 2005): G-0

450 \Rightarrow Modified extended hyperbolic model: C-0

451 \Rightarrow Manzari-Dafalias model: W-0 (Dafalias and Manzari, 2004)

452 In order to compare the different constitutive models, stress/strain controlled tests could have
453 been conducted. However, some of the teams were not able to perform it. To overcome this
454 difficulty, we asked the teams to compute nonlinear simulations with their codes on one of the
455 idealized soil profile (P1) with a sinus input motion of increasing amplitude and with a rigid
456 substratum base (Figure 4). The frequency of the input motion being low enough to avoid any
457 issues with wave propagation. Moreover, the result of such simulation was asked at the node
458 before the soil/bedrock interface, having a strength of 65 KPa.

459 The resulting plots are illustrated in Figure 5 for the total length of motion and in Figure 6 for
460 a specific zoom on the first two cycles (blue for the first and red for the second).

461 The full duration of motion leads to very high strain levels (5%), and the stress-strain curves
462 are highly variable from one computation to another. Even for a similar constitutive model,
463 the curves can differ. For Iwan's model U-0 and Y-0 results are close one to another while
464 different from K-0 and Q-0. The shape of the curves depends also on the use or not of
465 damping control. For instance, teams A-0, B-0, D-0, E-0, J-0, T-0 and F-0 used damping
466 control and all curves exhibit stress-strain curves with secant modulus degrading with strain.
467 Note that J-1 is an equivalent linear method and the stress-strain curves do not exhibit
468 hysteresis.

469 Some teams could not follow the prescribed shear strength values (M-0, M-1, M-2, R-0, S-0,
470 W-0) mainly because of depth dependency of the shear strength implemented in the code.
471 They used very different values; the comparison of the corresponding stress-strain curve is
472 thus irrelevant. Therefore, we looked at the first two cycles of motion that involve much
473 lower strain (not exceeding 0.5%): the stress-strain curves are closer to each another although
474 some indicate larger hysteresis loop (B-0) or lower maximal shear strain (Z-1). This
475 comparison helped to draw the attention on the lack of versatility of some of the used NL

476 codes, because of some built-in features based on empirical correlations or geotechnical
477 relations (between the shear strength and the confining pressure, for instance), which prevent
478 from considering fully arbitrary sets of NL parameters.

479 *Figure 4 : Acceleration time history of the sinus motion with central 1s period*

480 *Figure 5 : Stress-strain curve for a soil element of shear strength 65kPa subjected to a sinusoidal input seismic*
481 *motion of 10s.*

482 *Figure 6 : Stress-strain curve for a soil element of shear strength 65kPa subjected to the first two cycles of a*
483 *sinusoidal input seismic motion.*

484 ***Code usage protocols***

485 **Reference frequency for visco-elastic damping (Maxwell/Zener Model)**

486 Relatively little is known about low-strain, intrinsic attenuation in real soils. Its traditional
487 implementation supposes frequency independent damping values. This is readily achieved
488 using the Kelvin-Voigt model when solving the wave propagation in the frequency domain
489 (Ishihara, 1996). Conversely, the Maxwell/Zener generalized body better describes inelastic
490 material properties in both the time and frequency domain solution of wave propagation
491 (Moczo et al., 2004). However, the use of this rheology implies a slight velocity dispersion to
492 fulfill the causality principle. It is therefore needed to carefully define a reference frequency
493 for the reference velocity value, especially when different numerical methods are compared
494 with one another (Peyrusse et al., 2014). *[This reference frequency must not be confused with*
495 *the frequency bandwidth definition of the quasi-constant Q value used in the frequency*
496 *independent attenuation method aforementioned, it should simply be within this frequency*
497 *bandwidth.]*

498 A reference frequency was thus defined for each profile, at which common velocity and
499 attenuation values were fixed. As indicated by some authors (Liu and Archuleta, 2006; Moczo

500 et al., 2004) the values of reference frequency used in most cases is close to 1 Hz (as many
501 3D computations including shallow, soft material, have rather low upper bound maximum
502 frequencies). On the other hand, it is often suggested to select a frequency close to the
503 frequency of interest. In our case, given the definition of the pulse-like motion, we chose a
504 reference frequency of 4 Hz, i.e. the central value of the input wavelet.

505 **Definition and implementation of the reference motion**

506 We tested two base conditions at the sediment-substratum interface: (i) an elastic base, and
507 (ii) a rigid base. The first condition corresponds to the usual hazard assessment studies, where
508 the rock ground motion is derived from deterministic or probabilistic analysis, and
509 corresponds to the design motion at the surface of an outcropping rock. The second one
510 corresponds to the case where a recording is obtained at depth within a down-hole array, and
511 is used to derive the motion at surface or shallower depths. Depending on the communities or
512 point of views, the implementation of input (or reference) motions into algorithms can be
513 quite different, indicating that the terms "input motion" or "reference motion" are not
514 understood in the same way by all the participants. For the seismological community, the
515 input motion is often seen as the seismic signal carried by the up-going incident wave, while
516 for the geotechnical community, it is often understood as the motion at a given reference rock
517 site, resulting from the total-wavefield (up-going and down-going waves): this reference site
518 may be either at rock surface (it then includes the free-surface effect), or at depth (for instance
519 the downhole sensor of a vertical array, which includes the interferences between the up-
520 going and down-going waves).

521 For the case of a perfectly rigid substratum, the reference input motion is the signal imposed
522 at the soil-bedrock interface. This definition was clear among all teams. It was not so clear for
523 the elastic substratum condition, whereby a more precise definition was required, since the

524 greatest differences in the first round results came from different understandings of the term
525 "input motion" by the various teams. The terminology must therefore be clearly stated:

526 - Outcrop motion: Seismic motion recorded at the surface and corresponding to free surface
527 conditions in the outcropping rock. For 1-D cases, with vertically propagating seismic waves
528 and homogeneous rock, this free-surface effect is simply a frequency-independent factor of 2,
529 with respect to the up-going wave signal.

530 - Surface motion: Seismic motion recorded at the free surface of a sedimentary site and
531 subjected to amplification effects.

532 - Within motion: Seismic motion recorded at depth, usually at a downhole site: in our case,
533 this location corresponds to the interface between sediment and rock substratum (i.e., $z = 20$,
534 100 and 50 m, for profiles P1, P2 and P3, respectively). This motion contains the total wave-
535 field composed of the incident up-going and reflected down-going waves.

536 - Incident motion: Seismic motion that is carried by the incoming waves just before they enter
537 the sedimentary filling. In our case, it is the seismic motion carried by the vertically incident
538 plane wave, and it cannot be measured directly.

539 Considering the confusion among the participants linked with different working traditions in
540 different communities, we decided to use the concepts of "outcrop" and "within" input
541 motions to define the "reference motion" at the downhole sensor, as recommended by Kwok
542 et al. (2008) and Stewart and Kwok (2009). In linear/equivalent linear/non-linear site response
543 analyses, two cases can be distinguished:

544 (1) if the reference motion is an outcrop recording, then one should use an elastic base
545 condition with an up-going wave carrying a signal equal to exactly half the outcropping
546 motion;

547 (2) if the reference motion is a within motion recorded by a downhole sensor, then one
548 should use a rigid base condition without modifying the input motion.

549 In order to avoid any ambiguity, we will systematically use the expression "reference motion"
550 which should be understood as detailed above for the elastic and rigid base conditions

551 **Comparison of predictions**

552 *Methodology of comparison*

553 The participants were asked to compute the acceleration and stress-strain time histories at
554 virtual sensors located at different depths within the soil profile. A total of ten virtual sensors
555 were selected for each profile, with a depth interval equal to 1/10th of the total soil thickness:
556 every 2 m for P1, every 10 m for P2 and every 5 m for P3. Acceleration and stress-strain
557 values should be computed at staggered points: from the very surface for acceleration, and
558 from half the depth interval for stress-strain values.

559 From the "raw" results provided by each participant, a comparative analysis was performed
560 on the computed acceleration time histories, transfer function, 5% pseudo-response spectra,
561 the depth distribution of peak shear strain and PGA, and the stress-strain plots at different
562 depths. Such comparisons were done for each profile, for each computational case (linear vs.
563 non-linear, elastic vs. visco-elastic soil behavior, and rigid vs. elastic substratum conditions)
564 and for the different input motions.

565 For the sake of simplicity and conciseness, the main section of the present article presents
566 results for only the P1 case. The P2 and P3 profiles are compared to P1 results in terms of
567 variability of the surface motion only, but the conclusions are based on the results from all
568 three profiles.

569 *Visco-elastic computations*

570 Figure 7 displays the comparison for the P1 profile of the surface acceleration for the pulse-
571 like motion under an elastic substratum condition, for the linear elastic computation for a
572 short window (3 s) of signal. All results converged towards the analytical solution calculated
573 with the Haskell-Thomson method (Haskell, 1953; Thomson, 1950), but this was achieved
574 only after the second iteration. There were indeed unexpected and significant discrepancies in
575 amplitude at the end of the first iteration, and that came from: (1) inconsistent implementation
576 and understanding of the term "input motion" (clarified as mentioned in the code usage
577 protocols), (2) problems with units, or (3) representations of soil properties. During the first
578 iteration, some phase discrepancies could be also identified, associated either to the assignment
579 of the "input motion" at different depths some distance below the sediment/rock interface
580 (which caused a constant time delay), or to increasing time delays for the late cycles, that
581 were associated to numerical dispersion.

582 *Figure 7: Comparison of the acceleration at the surface of P1 profile, for the pulse-like input motion,*
583 *for the linear elastic computation and for the elastic substratum case.*

584 Figure 8 shows the results of visco-elastic computations of the acceleration at the surface of
585 the pulse-like motion with a rigid substratum condition. The convergence was also obtained
586 after the second iteration, with minor corrections (similar to the ones observed for the elastic
587 case) and after having specified the reference frequency to be considered for the
588 implementation of damping. We chose a reference frequency of 4 Hz, which is exactly the
589 central frequency of the pulse-like motion (Figure 8).

590 *Figure 8 Comparison of the acceleration at the surface of P1 profile, for the pulse-like input motion,*
591 *for the linear visco-elastic computation and for the rigid substratum case.*

592 These unexpected issues were corrected after the first iteration to ensure a satisfactory
593 convergence. This should however raise our awareness on the possibility of such
594 misunderstandings and resulting errors, when site response computations are asked without
595 clear enough specifications about the definition of the reference motion.

596 *Non-linear computations*

597 Once agreement between the model predictions was reached for simple, linear cases for which
598 analytical solutions are available, the variability of the results of non-linear calculations can
599 be fully associated with differences in implementation of non-linear soil behavior.

600 Figure 9 compares the Fourier transfer functions (surface over reference bedrock motion) and
601 Figure 10 compares pseudo-response spectra at the surface for the P1 profile, with a rigid
602 substratum case. The subplots of these two figures illustrate the results for the high frequency
603 (HF) waveform scaled to the lowest (0.5 m/s^2) and largest PGA (5 m/s^2) (a and c,
604 respectively), and for the low frequency (LF) waveform scaled to the lowest and largest PGA
605 (0.5 m/s^2 – b, and 5 m/s^2 , d, respectively). The frequency content of the input motion and the
606 scaling of the input motion prove to have a large influence on the non-linear soil behavior in
607 the numerical simulations, and consequently on the variability of the results.

608 While the results from all teams exhibit a very satisfactory similarity (though larger than for
609 the visco-elastic case) for the HF waveform scaled to the lowest PGA (a), differences between
610 the model predictions are much greater for the highest PGA (c). This observation is more
611 pronounced when looking at the LF input motion. Even for the lowest PGA (b), the variability
612 increases significantly compared to the HF input motion, and it becomes very large for the
613 large amplitude LF motion (scaled to 5 m/s^2 , d).

614 The amount of variability between the results has been quantified through the calculation of
615 the standard deviation (in log10 unit) for each frequency value and is illustrated in Figure 11.
616 The variability is greater for the low frequency content input motion scaled to the highest
617 PGA except close to the first frequency peak of the linear transfer function. As expected,
618 strong non-linear soil behavior during this solicitation shifts the first frequency peak of the
619 transfer function to the low frequencies. The variability of the transfer function is similarly
620 shifted.

621 Such variability is strongly linked to the peak shear strain reached in the soil column. For the
622 LF input motion scaled to the highest PGA, the threshold shear strain above which the
623 numerical simulations can no longer be considered as reliable (according to their authors),
624 was reached by some codes. Indeed, some teams (L-1 and Z-0) consider a maximal reliable
625 deformation between 1 to 2%; while others consider their code to work well over a wide
626 range of deformation and are limited by the dynamic soil properties resolution only. For the
627 computations using the HF and LF motions scaled to the highest PGA, we observe that the
628 two equivalent linear methods (J-1 and Z-0) exhibit a very high de-amplification beyond 7
629 Hz, compared to the other simulations, which shows the classical over-damping limitation of
630 that method. For the last two cases (HF and LF accelerograms scaled to 5 m/s^2), the peak
631 shear strain values are illustrated in Figure 12. It was calculated for each code/team couple,
632 and for all the 10 sensor depths of the P1 profile. The largest peak strain values, largely
633 exceeding 1%, are reached at the deepest points for the LF input motion, while it remains
634 about 10 times smaller (max 0.3%) for the HF motion, despite the identical PGA values on
635 the input motion. Besides, given the shape of the G/G_{\max} and $\xi(\gamma)$ curves, one may notice that
636 the frequency-content of the input motion induced variability in the peak shear strain results
637 which correspond to an even larger variability in the G/G_{\max} and $\xi(\gamma)$ values. For instance, at
638 7m depth, the peak shear strain for the LF motion is between 0.02 to 1% while it is between

639 0.03 to 0.1% for the HF motion. This makes the G/G_{\max} varies from 0.28 for the LF motion to
640 0.8 for the HF motion. Thus, one may understand that the results will be very sensitive to the
641 details of the constitutive model and the way that G/G_{\max} and $\xi(\gamma)$ curves are approximated.

642 Incidentally, one may also notice that for P1, the peak shear strain occurs at the deepest point,
643 close to the sediment/bedrock interface. Indeed, wave propagation in nonlinear media is the
644 cumulative effect of impedance contrast at the soil-bedrock interface, material strength, and
645 intensity of the input motion. These combined effects make it difficult to analyze these results
646 even when they are numerical and consider simple soil geometry.

647 *Figure 9 : Comparison of the surface to reference Fourier spectra ratio, for the non-linear comparison using*
648 *for the left sub-graphs the high frequency input motion and for the right sub-graphs the low-frequency input*
649 *motion and with for the first line the weakest input motion PGA and the second line the highest input motion*
650 *PGA.*

651 *Figure 10 : Comparison of the acceleration pseudo-response spectra at the ground surface, for the non-linear*
652 *computation using for the left sub-graphs the high frequency input motion and for the right sub-graphs the*
653 *low-frequency input motion and with for the first line the weakest input motion PGA and the second line the*
654 *highest input motion PGA*

655 *Figure 11 : Standard deviation (in log unit) of the transfer function (left panel) and response spectra (right*
656 *panel) depending of the input motion used.*

657 *Figure 12 : Peak shear strain profiles reached at each depth by each team for the high and low frequency*
658 *reference motion scaled at the highest PGA level (5 m/s^2), for the profile 1 and for rigid substratum conditions*

659 **Epistemic uncertainty**

660 *Quantification of the variability of the results*

661 We quantified the variability between the simulations by the standard deviations (log10 units)
662 of several ground motion intensity parameters, starting with PGA values $[\sigma_{\text{PGA}}]$, and then

663 considering pseudo-response spectrum ordinates at different periods [$\sigma_{PSA(T)}$], peak strains
664 [$\sigma_{\gamma_{max}}$], and a few energy related quantities.

665 The PGA values at the surface are first compared with the empirical variability (i.e. single
666 station, within-event variability " Φ_{SS} "). Figure 13 illustrates the evolution of σ_{PGA} for the
667 surface site of P1 for the 5 different computational cases and the different reference motion
668 and boundary conditions. These are the linear-elastic, the linear-visco-elastic, and the non-
669 linear computations with the input motions scaled to the lowest (0.5 m/s^2), intermediate (1
670 m/s^2) and highest (5 m/s^2) PGA. The σ_{PGA} is calculated for the pulse-like, the HF and the LF
671 motions. The left subplot displays the results for the rigid substratum case (reference motion =
672 within motion at sediment-basement interface), while the right subplot stands for the elastic
673 substratum case (reference motion = outcropping rock motion). The most striking features of
674 these plots can be summarized as follows:

- 675 a) the (almost) systematic increase of σ_{PGA} with increasing PGA level, whatever the input
676 signal and the type of boundary conditions
- 677 b) the (almost) systematically larger values of σ_{PGA} for the LF input motion compared to
678 the HF input motion case (around twice greater for the three PGA values) : this
679 corresponds to the higher strains generated by the LF motion. A similar plot as a
680 function of peak strain instead of peak ground acceleration would exhibit a larger
681 continuity between results of both input waveforms
- 682 c) the larger σ_{PGA} values for non-linear computations compared to the linear case (except
683 for the very specific case of linear-elastic response with rigid boundary conditions,
684 discussed later)
- 685 d) the maximum obtained σ_{PGA} value (0.15) remains below the specific single-station,
686 within-event variability $\Phi_{SS,PGA}$ value for a site with a V_{S30} equivalent to P1
687 (Rodriguez-Marek et al., 2011), which is around 0.2. The uncertainties linked with the

688 NL simulations remain below the “natural” single site response variability. The latter
689 one however includes the sensitivity to the characteristics of the incident wavefield,
690 which is not accounted for here as only vertically incident plane waves are considered.
691 Nonetheless, the use PGA as a main metric is not enough. It is helpful to use spectral
692 accelerations at other periods as well.

693 Our results indicate an exceptionally high σ_{PGA} value for one linear computation, the linear-
694 elastic one with the HF reference motion and rigid boundary conditions. This computational
695 case is the simplest but also the most demanding for a propagating seismic wave. Considering
696 that no seismic attenuation (damping) is considered for this specific computation (in the
697 material or in the substratum), some codes usually use numerical attenuation to control real
698 motion amplitudes. Thus, the high uncertainty observed here reflects variability in the
699 implementation of the numerical damping for each code/team couple, together with the high
700 sensitivity to the configuration, with a non-zero Fourier content of the reference motion at
701 depth, at a frequency where destructive interferences between up-going and down-going
702 waves should result in a null motion.

703 *Figure 13 : Standard deviation (in log10 unit) of the PGA at the surface of the P1 profile, for the 5 different*
704 *computational cases (linear –elastic, linear visco-elastic, non-linear with input motion scaled to the lowest*
705 *(0.5m/s²), medium (1m/s²) and highest (5m/s²) PGA, for the pulse-like, the high frequency and the low*
706 *frequency content motions. The left sub-plot shows the results for the rigid substratum case and the right sub-*
707 *plot for the elastic substratum.*

708 We then explored the variability of various seismic intensity measures: (i) the response
709 spectra at the surface (SA) at three different periods (0.1, 1 and 3 s), (ii) the peak shear strain
710 at the bottom of the sediment layer (ϵ), (iii) the Cumulative Absolute Velocity (CAV), (iv) the
711 Arias Intensity (IA), (v) the root mean square acceleration (Arms), and (vi) the 5%-95%
712 Trifunac-Brady duration (DT). The tendencies are quite similar for the HF and LF motions,

713 but are sensitive to the sediment/substratum limit condition (elastic vs. rigid). Considering
714 that σ_{PGA} is greater for the LF motion, we choose that motion to illustrate the results in Figure
715 14.

716 For the rigid substratum case (left subplot), three groups of intensity parameters can be
717 identified. The first group is composed of duration-dependent intensity parameters, i.e., CAV,
718 IA and DT, which exhibit the largest σ values. The second group is composed of acceleration
719 parameters (PGA, SA(T), Arms) and characterized by a lower σ , especially for long period
720 [SA (T = 1 s)]. The third group consists only of the peak strain, with generally intermediate σ
721 values, which however exhibit the largest variability from one case to another. These three
722 groups can also be distinguished in the elastic substratum case (right subplot), for which the
723 largest case-to-case variability is also observed for the peak strain, exhibiting the highest σ for
724 the highest PGA values. The duration-dependent parameters of the first group are less
725 variable under elastic boundary conditions especially at low to intermediate PGA levels and
726 in the linear domain: rigid base conditions are very demanding for low damping materials,
727 which maps much more on duration than on peak values.

728 *Figure 14 : Standard deviation (in log unit) of the different intensity parameters for the P1 profile, for the 5*
729 *different computational cases (linear –elastic, linear visco-elastic, non-linear with input motion scaled to the*
730 *lowest (0.5m/s²), medium (1m/s²) and highest (5m/s²) PGA, for the low frequency content motion. The left*
731 *sub-graph shows the results for the rigid substratum case and the right sub-graph for the elastic substratum.*

732 The other profiles provided similar results as to the variability of predictions. As an example,
733 Figure 15 compares the PGA variability, for the LF motion and a rigid substratum case, for
734 the three profiles. The trends are similar for the three profiles: similar σ values, same
735 tendency to increase with PGA. These results also stand for the elastic substratum case, as
736 well as the fact that the variability σ is lower for the HF motion for the three profiles, by about
737 a factor of two compared to the LF motion.

738 *Figure 15 : Standard deviation (in log unit) of the PGA for the profile 1 2 and 3, for the 5 different*
739 *computational cases (linear –elastic, linear visco-elastic, non-linear with input motion scaled to the lowest*
740 *(0.5m/s²), medium (1m/s²) and highest (5m/s²) PGA, for the low frequency content motion and for the rigid*
741 *substratum case.*

742 ***Origins of the variability: Can it be reduced?***

743 **Definition of Groups and Sub-groups**

744 We considered four a priori ways to group the results according to some characteristics of the
745 numerical codes: (G1) implemented attenuation method, (G2) numerical scheme, (G3)
746 constitutive model, (G4) shape of the hysteretic curve according to (1) the ability to represent
747 the actual shear strength value (here at the bottom of P1), and (2) the use or not of Masing
748 rules for the loading/unloading path (damping control or not). Each group is further sorted
749 into several sub-groups as follows.

750 Case G1 concerns the implementation of linear, intrinsic damping, as defined in the first part
751 of this article. It is sub-divided into 3 sub-groups: (i) G1a: frequency-independent attenuation
752 (A-0, E-0, F-0, J-0, J-1, K-0, M-0, Q-0 and Z-0), (ii) G1b: Rayleigh damping (B-0, G-0, H-0,
753 L-1, M-1, R-0, S-0, T-0, W-0, Y-0 and Z-1), and (iii) G1c: low strain hysteretic damping (C-
754 0, N-0, D-0 and R-0).

755 Case G2 is based on the numerical discretization scheme, which is sub-divided into 2
756 subgroups: (i) G2a: finite-element (B-0, D-0, H-0, L-1, M-0, N-0, Q-0, R-0, S-0, T-0, U-0,
757 W-0, Y-0 and Z-1), and (ii) G2b: finite-difference (A-0, C-0, E-0, F-0, G-0, J-0, K-0, L-2, M-
758 2). A third sub-group could be considered G2c: consisting of equivalent linear codes working
759 in the frequency domain (J-1 and Z-0).

760 Case G3 is based on the constitutive model. To ensure sufficient teams within each group, we
761 split the code/team couple into 4 sub-groups according to the main constitutive model used:

762 (i) G3a: IaI's model (B-0, E-0, Q-0), (ii) G3b: Iwan's model (K-0, L-1, U-0, Y-0), (iii) G3c:
763 Philips and Hashash's model (F-0, J-0, L-2, M-2, T-0), and (iv) G3d: all other models.

764 Case G4 is based on the shape of the hysteresis loop according to (1) the shear strength used
765 by each code/team couple and (2) the use of Masing rules or not for the loading/unloading
766 path.

767 In the "canonical" models initially designed by the organizing team, the soil shear strength
768 profile was assumed to be constant with depth in each soil layer, and had prescribed modulus
769 reduction and damping curves. However, in most real situations, the shear strength should
770 increase with depth. Even though these profiles were considered as "idealized" and simply
771 intended to perform these verification tests, some teams felt very uncomfortable with this
772 unrealistic assumption and decided to change the shear strength profile, by introducing a more
773 realistic increase in shear strength with depth, having nevertheless, the imposed strength
774 values at the center of each layer. Consequently, the actual non-linear soil parameters
775 considered by each team were not identical, which is certainly responsible for part of the final
776 variability observed, especially for large ground motions, for which the actual strain and
777 damping are more sensitive to the shear strength than to the shear velocity, particularly at or
778 close to major interfaces. For this reason, we further sorted each code/team couple into 2 sub-
779 groups, by analyzing the stress-strain plots for the LF motion and the highest PGA at the
780 bottom of P1 (illustrated in Figure 16). We choose this computational case because it is the
781 most challenging in term of maximal shear strain reach in the soil column and therefore can
782 highlight the differences between the computations. We found the following sub-groups: (i)
783 shear strength is equal to 65kPa, as stated by the organizing team (A-0, B-0, C-0, E-0, F-0, G-
784 0, H-0, K-0, Q-0, U-0, T-0, Y-0), and (ii) all others that exceeded this value (D-0, J-0, J-1, L-
785 1, N-0, M-0, M-1, M-2, R-0, S-0, W-0, Z-0, Z-1).

786 In addition, we also consider the damping control implementation, (or in other words the use
787 or not of the Masing loading/unloading rules). It has a major influence on the hysteresis
788 curves and hence on the non-linear soil behavior, also illustrated in Figure 16. It is split into 2
789 sub-groups: (i) damping control is used, i.e. the Masing rules are not applied (A-0, B-0, E-0,
790 F-0, J-0, M-2), and (ii) no damping control used (all other teams).

791 Combining these two last parameters we end-up for G4 with three subgroups as follow: (i)
792 G4-a: Specified shear strength and use of damping control (A-0, B-0, E-0, F-0, T-0), (ii) G4-
793 b: Specified shear strength and no use of damping control and (C-0, G-0, H-0, K-0, Q-0, U-0,
794 Y-0) (iii) G4-c: Different shear strength (D-0, J-0, J-1, L-1, N-0, M-0, M-1, M-2, R-0, S-0,
795 W-0, Z-0, Z-1).

796 *Figure 16 : Stress-strain curves at the bottom of P1 Profile for the Rigid substratum case subjected to the low*
797 *frequency motion (in color and the high frequency motion in black scaled to the highest PGA (5m/s²). The*
798 *grey curves are for code/team couples that exceed the specified shear strength of 65 KPa, whereas the*
799 *coloured curves represent the code/team couples that use 65 KPa. The red curves are for codes using damping*
800 *control and the blue curves the others.*

801 **Variability within the sub-groups**

802 Considering the level of code-to-code variability, and its increase with PGA or strain level, a
803 major issue regarding non-linear computations is whether such variability, i.e. the uncertainty
804 in the predicted motion, is intrinsic to these kinds of calculations, or can be reduced, and in
805 the latter case, how? We thus looked at the variability within each subgroup of the four main
806 grouping, in order to identify those, which are associated to a significantly reduced scatter.

807 The standard deviations (σ_{\log} , calculated in \log_{10} units) of three parameters describing the
808 computed surface accelerations and the strain levels at the bottom of P1, were used as a
809 metrics to validate the ability of a given grouping item to reduce the scatter of results. These
810 parameters are the surface PGA and the acceleration response spectra (RS) at periods 0.3 s

811 and 0.09 s (corresponding to P1's first and second resonance frequencies, respectively). For
812 each, the variability was measured within each subgroup of the 4 groups. If the groupings are
813 physically relevant, the within-subgroup variability should be significantly reduced.

814 Figure 17 shows the standard deviation values for each sub-group in each group (G1, G2, G3
815 and G4) relative to the general standard deviation (all unsorted code/team couples) illustrated
816 by the dotted gray line. The standard deviation of the PGA, response spectra at two periods
817 and maximal deformation are calculated on the results for the profile P1, with the rigid
818 substratum case and using the low frequency input motion scaled to the highest PGA (i.e. the
819 motion that induces the strongest deformation in the soil column).

820 G1 and G2 (i.e. low strain attenuation and numerical scheme implementation, respectively) do
821 not exhibit much lower σ_{\log} values compared to the general σ_{\log} , except for the lowest PGA
822 input motion. Conversely, G3 to G4 (i.e. constitutive model, shear strength and damping
823 control groups) do show reduced σ_{\log} relative to the general σ_{\log} , with G4 demonstrating the
824 strongest reductions (by at least a factor of 2).

825 We can therefore conclude that (i) the shear strength is a key parameter for non-linear
826 computations, and (ii) the constitutive model has a large influence; however (iii) the use (or
827 not) of Masing rules appears to have an even greater influence for strong input motion.

828 *Figure 17 : Standard deviation values (σ_{\log} , in \log_{10} units) of four parameters for the non-linear computation*
829 *using the low-frequency content input motion scaled to the highest PGA : PGA (upper left), Response spectra*
830 *at 0.27 s (upper right), Response spectra at 0.09 s (lower left) all three at the surface of P1 and the maximal*
831 *shear deformation at the bottom of the P1 profile (lower right). The standard deviation are given for each*
832 *group of the four groupings: depending on their low strain attenuation implementation (G-1) their numerical*
833 *scheme (G-2) their constitutive models (G-3) and their values of shear strength at the bottom of P1 and use of*
834 *damping control or not (G-5). The grey area illustrates the standard deviation for all code/team couples.*

835 Figure 18 compares the pseudo-acceleration response spectra at the surface of the P1 profile
836 with a rigid substratum condition subjected to LF and HF input motions scaled at the medium
837 (1m/s^2) and highest (5 m/s^2) PGA levels. The response spectra are sorted according to the G4
838 sub-grouping, and the associated σ_{\log} is represented by the thin lines on top of each subplot
839 (the numbers on the right side indicate the number of code/team pairs in each sub-group). G4
840 enables a clear distinction of the response spectra; particularly for the most demanding LF
841 input motion. The σ_{\log} values from the two sub-groups with identical τ_{\max} (G4a and G4b) are
842 considerably reduced below 2 s, compared to the rest of the computations (G4c). This period
843 bandwidth is relative to the PGA of this LF input motion. Similarly, for the HF input motion,
844 the σ is reduced below 1 s.

845 Besides, the response spectra computed for the strongest input motions (HF and LF) at the
846 surface of groups G4a and G4b are significantly different one to another which show the large
847 impact of using damping control or not. The response spectra computed with damping control
848 are more damped at intermediate frequencies (period between [0.2 to 0.7] s and [0.2 to 1] s for
849 the HF and LF motion respectively) and less attenuated at low frequencies (periods greater
850 than 0.7 and 1 s for the HF and LF motion respectively).

851 *Figure 18 : Comparison of the pseudo- acceleration response spectra at the ground surface of P1 with rigid*
852 *substratum condition, for the non-linear computation using for the left sub-graphs the high frequency input*
853 *motion and for the right sub-graphs the low-frequency input motion and with for the first line the middle*
854 *input motion PGA and the second line the highest input motion PGA. The response spectra were sorted*
855 *according to three groups: group 1 is composed of the code/team couples using similar τ_{\max} and damping*
856 *control constitutive model. Group 2 use similar τ_{\max} and no damping control and Group 3 are the other code*
857 *team couples.*

858 **Conclusions**

859 In the PRENOLIN's verification phase, the linear computation involving a simple pulse-like
860 (Ricker) input motion proved to be very useful in understanding and eliminating some of the
861 discrepancies between the different numerical codes that were compared. It was found that
862 code-to-code differences can be attributed to three different sources: (1) minor mistakes in
863 input parameter implementation or output units, (2) different understanding of the expression
864 "input motion" within different communities, and (3) different intrinsic attenuation and
865 numerical integration implementations. This benchmark showed that any nonlinear code
866 should be tested with simple linear cases before going into nonlinear computations to ensure
867 the proper implementation of the elastic soil parameters.

868 Most of the codes tested in this verification benchmark were designed mainly for non-linear
869 computations. Therefore, although the codes should well reproduce the soil behavior at low
870 strains, their actual performance are mainly tested for their soil behavior predictions during
871 strong shaking in real cases.

872 The results obtained so far indicate a code-to-code variability, which increases with the shear
873 strain level (which in turn depends on both the PGA level, stiffness of the soil and the
874 frequency content of the reference input motion). We also found that, whatever the soil
875 profiles used (among the 3 soil profiles considered), the overall code-to-code variability in the
876 worst case (with strain levels exceeding 1%) remained lower than the random variability of
877 GMPE single-station σ values for PGA. Nevertheless, an important conclusion is that given
878 the scatter in the nonlinear results, a realistic analysis should use more than one code to
879 perform a site response computation.

880 The effect of different non-linear soil model implementations was explored in this study and
881 our main observations indicate that the epistemic uncertainty (i.e. the code-to-code

882 variability) can be significantly reduced by describing more precisely some specific input
883 parameters, especially the soil shear strength profile, which is found to be a key specification
884 in addition to the degradation curves. In addition, for one particular non-linear soil model
885 implemented in different codes (Iai's model), the variability of the stress-strain curves were
886 found to be large, and mainly caused by the damping control parameter, depending on
887 whether it was used to simultaneously fit the strain-dependence of both shear modulus and
888 damping, or not, in order to follow the Masing loading/unloading rules. All these features and
889 conclusions need to be checked against actual data to provide support for defining best
890 practice for modeling out of the many available: vertical arrays with multiple down-hole
891 sensors are the best available in-situ instrumentations to go forward. The benchmark
892 undoubtedly benefits a lot from the various expertise fields of the participants ranging from
893 geotechnical earthquake engineering to engineering seismology.

894 **Data and resources**

895 Time histories used in this study were collected from the KiK-net web site
896 www.kik.bosai.go.jp and <http://www.kik.bosai.go.jp/kik/> (last accessed November 2011)
897 and from University of Iceland, Engineering Research Institute, Applied Mechanics
898 Laboratory, Reykjavik, Iceland.

899 **Acknowledgements**

900 Such an exercise was made possible by the interest and funding of the French and Italian
901 nuclear industry under the project "SIGMA". It was made successful thanks to the dedicated
902 and proactive participation of many teams from all over the world: A large number of teams
903 reacted very positively to our invitation to take part in this (risky) benchmarking exercise,

904 among them the developers of a wide variety of internationally used constitutive laws and/or
905 codes. Such a broad participation witnesses the actual need for such a carefully controlled
906 comparison, and also brought an invaluable enrichment to the project, which undoubtedly
907 benefitted greatly from the deep expertise of the participants. PRENOLIN is part of two larger
908 projects: SINAPS@, funded by the ANR (the French National Research Agency), and
909 SIGMA, funded by a consortium of nuclear operators (EDF, CEA, AREVA, ENL).

910

911

912 **References**

- 913 Aki, K., Richards, P.G., 2002. Quantitative seismology.
- 914 Aubry, D., Hujeux, J.C., Lassoudiere, F., Meimon, Y., 1982. A double memory model with
915 multiple mechanisms for cyclic soil behaviour, in: Proceedings of the Int. Symp. Num. Mod.
916 Geomech. pp. 3–13.
- 917 Aubry, D., Modaressi, A., 1996. GEFDYN, Manuel scientifique. Éc. Cent. Paris LMSS-Mat.
- 918 Bardet, J.P., Ichii, K., Lin, C.H., 2000. EERA: a computer program for equivalent-linear
919 earthquake site response analyses of layered soil deposits. University of Southern California,
920 Department of Civil Engineering.
- 921 Benz, T., 2006. Small strain stiffness of soils and its consequences. Dr. Thesis IGS Univ.
922 Stuttg.
- 923 Benz, T., Vermeer, P.A., Schwab, R., 2009. A small-strain overlay model. Int. J. Numer.
924 Anal. Methods Geomech. 33, 25–44.
- 925 Beresnev, I.A., Wen, K.-L., Yeh, Y.T., 1995. Nonlinear Soil Amplification: Its Corroboration
926 in Taiwan. Bull. Seismol. Soc. Am. 85, 456–515.
- 927 Biot, M.A., 1956. Theory of Propagation of Elastic Waves in a Fluid-Saturated Porous Solid.
928 I. Low-Frequency Range. J. Acoust. Soc. Am. 28, 168–178. doi:10.1121/1.1908239
- 929 Blanch, J.O., Robertsson, J.O., Symes, W.W., 1995. Modeling of a constant Q: Methodology
930 and algorithm for an efficient and optimally inexpensive viscoelastic technique. Geophysics
931 60, 176–184.
- 932 Bonilla, L.F., Archuleta, R.J., Lavallée, D., 2005. Hysteretic and Dilatant Behavior of
933 Cohesionless Soils and Their Effects on Nonlinear Site Response: Field Data Observations
934 and Modeling. Bull. Seismol. Soc. Am. 95, 2373–2395.
- 935 Boore, D.M., Bommer, J.J., 2005. Processing of strong-motion accelerograms: needs, options

936 and consequences. *Soil Dyn. Earthq. Eng.* 25, 93–115.

937 Cundall, P., 2006. A simple hysteretic damping formulation for dynamic continuum
938 simulations, in: *Proceedings of the 4th International FLAC Symposium on Numerical*
939 *Modeling in Geomechanics*. Minneapolis: Itasca Consulting Group.

940 Dafalias, Y.F., Manzari, M.T., 2004. Simple plasticity sand model accounting for fabric
941 change effects. *J. Eng. Mech.* 130, 622–634.

942 Darendeli, M.B., 2001. Development of a new family of normalized modulus reduction and
943 material damping curves.

944 Day, S.M., Bradley, C.R., 2001. Memory-efficient simulation of anelastic wave propagation.
945 *Bull. Seismol. Soc. Am.* 91, 520–531.

946 Day, S.M., Minster, J.B., 1984. Numerical simulation of attenuated wavefields using a Padé
947 approximant method. *Geophys. J. Int.* 78, 105–118.

948 Derras, B., Bard, P.-Y., Cotton, F., Bekkouche, A., 2012. Adapting the Neural Network
949 Approach to PGA Prediction: An Example Based on the KiK-net Data. *Bull. Seismol. Soc.*
950 *Am.* 102, 1446–1461.

951 Elgamal, A., Yang, Z., Parra, E., Ragheb, A., 2003. Modeling of cyclic mobility in saturated
952 cohesionless soils. *Int. J. Plast.* 19, 883 – 905. doi:[http://dx.doi.org/10.1016/S0749-](http://dx.doi.org/10.1016/S0749-6419(02)00010-4)
953 [6419\(02\)00010-4](http://dx.doi.org/10.1016/S0749-6419(02)00010-4)

954 Foerster, E., Gélis, C., De Martin, F., Bonilla, L.-F., 2015. Numerical study of 1D/2D wave
955 propagation in the Mygnodian basin, EUROSEISTEST, Northern Greece. 9ème Colloq.
956 AFPS.

957 Gerolymos, N., Gazetas, G., 2006. Winkler model for lateral response of rigid caisson
958 foundations in linear soil. *Soil Dyn. Earthq. Eng.* 26, 347–361.

959 Gerolymos, N., Gazetas, G., 2005. Constitutive model for 1-D cyclic soil behaviour applied to
960 seismic analysis of layered deposits. *Soils Found.* 45, 147–159.

961 Graves, R.W., Day, S.M., 2003. Stability and accuracy analysis of coarse-grain viscoelastic
962 simulations. *Bull. Seismol. Soc. Am.* 93, 283–300.

963 Hashash, Y.M.A., Groholski, D.R., Phillips, C.A., Park, D., Musgrove, M., 2012. DEEPSOIL
964 5.1. User Man. Tutor. 107.

965 Haskell, N.H., 1953. The dispersion of surface waves in multilayered media. *Bull. Seismol.*
966 *Soc. Am.* 43, 17–34.

967 IAI, S., MATSUNAGA, Y., KAMEOKA, T., 1992. Strain space plasticity model for cyclic
968 mobility. *SOILS Found.* 32, 1–15. doi:10.3208/sandf1972.32.2_1

969 Iai, S., Morita, T., Kameoka, T., Matsungaya, Y., Abiko, K., 1995. Response of a dense sand
970 deposit during 1993 Kushiro-Oki earthquake. *Soils Found.* 35, 115–131.

971 Iai, S., Ozutsumi, O., 2005. Yield and cyclic behaviour of a strain space multiple mechanism
972 model for granular materials. *Int. J. Numer. Anal. Methods Geomech.* 29, 417–442.
973 doi:10.1002/nag.420

974 Iai, S., Tobita, T., Ozutsumi, O., Ueda, K., 2011. Dilatancy of granular materials in a strain
975 space multiple mechanism model. *Int. J. Numer. Anal. Methods Geomech.* 35, 360–392.
976 doi:10.1002/nag.899

977 Ishibashi, I., Zhang, X., 1993. Unified Dynamic shear moduli and damping ratio of sand and
978 clay. *Soils Found.* 33, 182–191.

979 Ishihara, K., 1996. *Soil Behaviour in Earthquake Geotechnics*. Clarenton Press, Oxford.

980 ITASCA, F., 2011. 7.0: User Manual. Licence Number 213-039-0127-18973. Sapienza—
981 Univ Rome Earth Sci. Dep.

982 Iwan, W.D., 1967. On a class of models for the yielding behavior of continuous and
983 composite systems. *J. Appl. Mech.* 34, 612–617.

984 Johnston, D.H., Toksoz, M.N., Timur, A., 1979. Attenuation of seismic waves in dry and
985 saturated rocks; II, Mechanisms. *Geophysics* 44, 691–711. doi:10.1190/1.1440970

986 Kontoe, S., 2006. Development of time integration schemes and advanced boundary
987 conditions for dynamic geotechnical analysis. Imperial College London (University of
988 London).

989 Kwok, A.O., Stewart, J.P., Hashash, Y.M., 2008. Nonlinear ground-response analysis of
990 Turkey Flat shallow stiff-soil site to strong ground motion. *Bull. Seismol. Soc. Am.* 98, 331–
991 343.

992 Leurer, K.C., 1997. Attenuation in fine-grained marine sediments; extension of the Biot-Stoll
993 model by the “effective grain model” (EGM). *Geophysics* 62, 1465–1479.
994 doi:10.1190/1.1444250

995 Liu, P., Archuleta, R.J., 2006. Efficient Modeling of Q for 3D Numerical Simulation of Wave
996 Propagation. *Bull. Seismol. Soc. Am.* 96, 1352–1358. doi:10.1785/0120050173

997 Matasovic, N., Kavazanjian Jr, E., 2006. Seismic response of a composite landfill cover. *J.*
998 *Geotech. Geoenvironmental Eng.* 132, 448–455.

999 Matasović, N., Ordóñez, G., 2007. D-MOD2000. GeoMotions, LLC, Computer Software.

1000 Matasovic, N., vucetic, M., 1995. Generalized cyclic-degradation-pore-pressure generation
1001 model for clays. *J. Geotech. Eng.* 121, 33–43.

1002 Matasovic, N., vucetic, M., 1993. Analysis of seismic records obtained on november 24, 1987
1003 at the Wildlife liquefaction array. University of California, Los Angeles.

1004 Mercerat, E.D., Glinsky, N., 2015. A nodal discontinuous Galerkin method for non-linear soil
1005 dynamics. 6th Int. Conf. Earthq. Geotech. Eng.

1006 Moczo, P., Kristek, J., Gális, M., 2004. Simulation of the planar free surface with near-
1007 surface lateral discontinuities in the finite-difference modeling of seismic motion. *Bull.*
1008 *Seismol. Soc. Am.* 94, 760–768.

1009 Modaressi, H., Foerster, E., 2000. CyberQuake. User’s Man. BRGM Fr.

1010 Olsen, K., Day, S., Bradley, C., 2003. Estimation of Q for long-period (> 2 sec) waves in the

1011 Los Angeles basin. *Bull. Seismol. Soc. Am.* 93, 627–638.

1012 Peyrusse, F., Glinsky, N., Gélis, C., Lanteri, S., 2014. A high-order discontinuous Galerkin
1013 method for viscoelastic wave propagation, in: *Spectral and High Order Methods for Partial*
1014 *Differential Equations-ICOSAHOM 2012*. Springer, pp. 361–371.

1015 Phillips, C., Hashash, Y.M.A., 2009. Damping formulation for nonlinear 1D site response
1016 analyses. *Soil Dyn. Earthq. Eng.* 29, 1143 – 1158.
1017 doi:<http://dx.doi.org/10.1016/j.soildyn.2009.01.004>

1018 Pisanò, F., Jeremić, B., 2014. Simulating stiffness degradation and damping in soils via a
1019 simple visco-elastic–plastic model. *Soil Dyn. Earthq. Eng.* 63, 98–109.

1020 Potts, D.M., Zdravkovic, L., 1999. *Finite element analysis in geotechnical engineering:*
1021 *theory*. Imperial College of Science, Technology and Medicine. Thomas Telford Publishing,
1022 Thomas Telford Ltd, ISBN 0-7277-2783-4.

1023 Puzrin, A.M., Shiran, A., 2000. Effects of the constitutive relationship on seismic response of
1024 soils. Part I. Constitutive modeling of cyclic behavior of soils. *Soil Dyn. Earthq. Eng.* 19, 305
1025 – 318. doi:[http://dx.doi.org/10.1016/S0267-7261\(00\)00027-0](http://dx.doi.org/10.1016/S0267-7261(00)00027-0)

1026 Régnier, J., Cadet, H., Bonilla, L., Bertand, E., Semblat, J.F., 2013. Assessing nonlinear
1027 behavior of soil in seismic site response: Statistical analysis on KiK-net strong motion data.
1028 *Bull. Seismol. Soc. Am.* 103, 1750–1770.

1029 Rodriguez-Marek, A., Mantalva, G. 1, Cotton, F., Bonilla, F., 2011. Analysis of Single-
1030 Station Standard Deviation Using the KiK-net Data. *Bull. Seismol. Soc. Am.* 101, 1242–
1031 1258.

1032 Sandikkaya, M.A., Akkar, S., Bard, P.-Y., 2013. A Nonlinear Site-Amplification Model for
1033 the Next Pan-European Ground-Motion Prediction Equations. *Bull. Seismol. Soc. Am.* 103,
1034 19–32.

1035 Santisi d'Avila, M.P., Lenti, L., Semblat, J.-F., 2012. Modelling strong seismic ground

1036 motion: three-dimensional loading path versus wavefield polarization. *Geophys. J. Int.* 190,
1037 1607–1624.

1038 Santisi d’Avila, M.P., Semblat, J.-F., 2014. Nonlinear seismic response for the 2011 Tohoku
1039 earthquake: borehole records versus one-directional three-component propagation models.
1040 *Geophys. J. Int.* 197, 566–580.

1041 Santisi d’Avila, M.P., Semblat, J.-F., Lenti, L., 2013. Strong Ground Motion in the 2011
1042 Tohoku Earthquake: A One-Directional Three-Component Modeling. *Bull. Seismol. Soc.*
1043 *Am.* 103, 1394–1410.

1044 Schanz, T., Vermeer, P.A., Bonnier, P.G., 1999. The hardening soil model: formulation and
1045 verification. *2000 Comput. Geotech.* 281–296.

1046 Schnabel, P.B., Lysmer, J., Seed, H.B., 1972. SHAKE : a computer program for earthquake
1047 response analysis of horizontally layered sites (report). Earthquake Engineering Research
1048 Centre, Berkeley, California.

1049 Seed, H., 1969. 1. M. Idriss, Influence of soil conditions on ground motions during
1050 earthquakes, *J. Soil Mech Found Div Amer Soc Civ Eng* 95.

1051 Semblat, J.F., 1997. Rheological Interpretation of Rayleigh Damping. *J. Sound Vib.* 206,
1052 741–744. doi:10.1006/jsvi.1997.1067

1053 Stewart, J., Kwok, A., 2009. Nonlinear Seismic Ground Response Analysis: Protocols and
1054 VerificaBon Against Array Data. *PEER Annu. Meet. San Franc.-Present.* 84.

1055 Susumu Iai, T.K., Yoasuo Matsunaga, 1990. Strain space plasticity model for cyclic mobility
1056 (No. 4). port and harbour reasearch insitute.

1057 Taborda, D.M., Zdravkovic, L., Kontoe, L., Potts, D.M., 2010. Alternative formulations for
1058 cyclic nonlinear models: parametric study and comparative analyses. *Numer. Methods*
1059 *Geotech. Eng. NUMGE 2010 Benz Nord.* Eds CRC Press, 423–428.

1060 Thomson, W.T., 1950. Transmission of elastic waves through a stratified solid. *J. Appl. Phys.*

1061 21, 89–93.

1062 Tropeano, G., Chiaradonna, A., onofrio, A. d', Sivistri, F., 2015. An innovative computer
1063 code for 1D seismic response analysis including shear strength of soils. 101680geotSIP 15-P-
1064 017.

1065 Vucetic, M., Dobry, R., 1991. Effect of soil plasticity on cyclic response. J. Geotech. Eng.
1066 117.

1067 Yang, Z., Elgamal, A., Parra, E., 2003. Computational model for cyclic mobility and
1068 associated shear deformation. J. Geotech. Geoenvironmental Eng. 129, 1119–1127.

1069 Yu, G., Anderson, J.G., Siddharthan, R.A.J., 1993. On the characteristics of nonlinear soil
1070 response. Bull. Seismol. Soc. Am. 83, 218–244.

1071 Zeghal, M., Elgamal, A.-W., Tang, H.T., Srepp, J.C., 1995. Lotung downhole array. II:
1072 Evaluation of soil nonlinear properties. J. Geotech. Eng. 121, 363–378.

1073

1074

1075

1076 **TABLES**

1077 *Table 1: Soil properties for all three simple profile cases studied here (P1-3), for the elastic and non-elastic*
 1078 *domains.*

| Profile | LINEAR | | | | | | | | | NL |
|--|--------|----------|----------|-----------------------------|-----------|----------------------|-----------------|----------------------------|------------------------------------|--------|
| | Z [m] | Vs [m/s] | Vp [m/s] | ρ [kg/m ³] | Q Elastic | ξ_{\min} Elastic | Q Visco-Elastic | ξ_{\min} Visco-Elastic | F ₀ Linear Elastic [Hz] | |
| P1 | 0-20 | 300 | 700 | 2000 | 5000 | 10 ⁻⁴ | 30 | 0.0166 | 3.75 | N°1-P1 |
| | - | 1000 | 1900 | 2500 | | | 200 | 0.0025 | | - |
| P2 Mono-layer + V _{gradient} | 0-20 | 150-500 | 360-1220 | 2000 | | | 34 | 0.0154 | 1.16 | N°1-P2 |
| | 20-40 | | | | | | 40 | 0.0250 | | N°2-P2 |
| | 40-60 | | | | | | 44 | 0.0113 | | N°3-P2 |
| | 60-80 | | | | | | 47 | 0.0106 | | N°4-P2 |
| | 80-100 | | | | | | 49 | 0.0102 | | N°5-P2 |
| | - | 200 | 0.0025 | - | | | | | | |
| P3 Bi-layer | 0-20 | 300 | 700 | 2000 | | | 30 | 0.0166 | 1.48 | N°1-P3 |
| | 20-100 | 600 | 1500 | 2000 | | | 60 | 0.0083 | | N°2-P3 |
| | - | 2000 | 3700 | 2500 | 200 | 0.0025 | - | | | |

1079

1080 *Table 2 Seismic metadata of the two real input motions used in the verification phase of the Prenolin project.*

| Event Freq. Content | Event ID | Mw | Z [km] | Epi. Dist. [km] | Station ID | Station Geology | Seismo Comp. | Vs30 [m/s] Mean harmonic S-waves velocity over the first 30m depth |
|---------------------|-------------------|-----|--------|-----------------|---------------------------|-----------------|--------------|---|
| HF | IWTH-170112022202 | 6.4 | 122 | 39 | IWTH17 (Kik-net, Japan) | Rock | EW | >1200 |
| LF | 06756.20000617 | 6.6 | 15 | 5 | Flagbjarnarholt (Iceland) | A | H1 | Unknown |

1081

1082

Table 3: Participants to the PRENOLIN project Verification phase.

| Team Name | Affiliation | Team Index | Code Name | Code Reference |
|--|--|------------|--------------------------|---|
| <i>D. Assimaki & J. Shi</i> | <i>Georgia tech, US</i> | A 0 | GEORGIA-NL-FDM | (Matasovic and Kavazanjian Jr, 2006; Matasovic and vucetic, 1993) |
| <i>S. Iai</i> | <i>DPRI, Japan Univ.</i> | B 0 | FLIP | (Susumu Iai, 1990) |
| <i>S. Kramer</i> | <i>Washington, US</i> | C 0 | PSNL | (In development) |
| <i>E. Foerster</i> | <i>CEA, France</i> | D 0 | CYBERQUAKE | (Modaressi and Foerster, 2000) |
| <i>C. Gelis</i> | <i>IRSN, France</i> | E 0 | NOAH-2D | (Susumu Iai, 1990) |
| <i>A. Giannakou</i> | <i>Fugro, France</i> | F 0 | DEEPSOIL 5.1 | (Hashash et al., 2012) |
| <i>G. Gazetas E. Garini & N. Gerolymos</i> | <i>NTUA, Greece</i> | G 0 | NL-DYAS | (Gerolymos and Gazetas, 2006, 2005) |
| <i>J. Gingery</i> | <i>UCSD, US</i> | H 0 | OPENSEES-UCSD-SOIL-MODEL | (http://opensees.berkeley.edu/) |
| <i>Y. Hashash & J. Harmon</i> | <i>Univ, Illinois, US</i> | J 0 | DEEPSOIL-NL 5.1 | (Hashash et al., 2012) |
| | | J 1 | DEEPSOIL-EL 5.1 | (Hashash et al., 2012) |
| <i>P. Moczo, J. Kristek & A. Richterova</i> | <i>CUB</i> | K 0 | 1DFD-NL-IM | ... |
| <i>S. Foti & S. Kontoe</i> | <i>Politecnico di Torino & Imperial College, Italy</i> | L 1 | ICFEP | (Kontoe, 2006; Potts and Zdravkovic, 1999; Taborda et al., 2010) |
| | | L 2 | DEEPSOIL-NL 5.1 | (Hashash et al., 2012) |
| | | M 0 | FLAC_7,00 | (ITASCA, 2011) |
| <i>G. Lanzo, S. Suwal, A. Pagliaroli & L. Verrucci</i> | <i>Univ. Rome La Sapienza, Italy</i> | M 1 | DMOD2000 | (Matasović and Ordóñez, 2007) |
| | | M 2 | DEEPSOIL 5.1 | (Hashash et al., 2012) |
| <i>F. Lopez-Caballero & S. Montoya-Noguera</i> | <i>ECP, France</i> | N 0 | GEFDyn | (Aubry and Modaressi, 1996) |
| <i>F. De-Martin</i> | <i>BRGM, France</i> | Q 0 | EPISPEC1D | (Iai, 1990) http://efispec.free.fr |

| | | | | | |
|--|---|---|---|---------------------|---|
| <i>B. Jeremić, F. Pisanò & K. Watanabe</i> | <i>UCD, LBLN, TU Delft & Shimizu Corp</i> | R | 0 | real ESSI Simulator | http://sokocalo.engr.ucdavis.edu/~Jeremić/Real_ESSI_Simulator/ |
| <i>A. Nieto-Ferro</i> | <i>EDF, France</i> | S | 0 | ASTER | http://www.code-aster.org |
| <i>A. Chiaradonna, F. Silvestri & G. Tropeano</i> | <i>UNICA and Univ. Naples, Italy</i> | T | 0 | SCOSSA_1,2 | (Tropeano et al., 2015) |
| | | T | 1 | STRATA | |
| <i>M.P. Santisi d'Avila</i> | <i>Univ. Nice Sophia-Antipolis, France</i> | U | 0 | SWAP_3C | (Santisi d'Avila et al., 2012, 2013; Santisi d'Avila and Semblat, 2014) |
| <i>D. Mercerat and N. Glinsky</i> | <i>CEREMA, France</i> | Y | 0 | DGNL | (Mercerat and Glinsky, 2015) |
| <i>D. Boldini, A. Amorosi, A. di Lernia & G. Falcone</i> | <i>Univ. Bologna and Sapienza University of Rome, Italy</i> | Z | 0 | EERA | (Bardet et al., 2000) |
| | | Z | 1 | PLAXIS | (Benz, 2006; Benz et al., 2009) |
| <i>M. Taiebat & P. Arduino</i> | <i>Univ. Vancouver, Canada</i> | W | 0 | Opensees | (http://opensees.berkeley.edu/) |

1085

1086

1087 **List of Figures**

1088 Figure 1 : The three simple idealized profile cases studied here (P1-3), for the elastic and
1089 non-elastic domains, and for a rigid and elastic soil-bedrock base, using a Ricker
1090 pulse and 3 accelerations of different PGA and frequency contents. 11

1091 Figure 2 : Vs profiles, G/G_{max} and damping curves for the 3 idealized profiles. 16

1092 Figure 3: Normalized reference motion used for the verification phase of this project
1093 PRENOLIN..... 17

1094 Figure 4 : Acceleration time history of the sinus motion with central 1s period 24

| | | |
|------|--|----|
| 1095 | Figure 5 : Stress-strain curve for a soil element of shear strength 65kPa subjected to a | |
| 1096 | sinusoidal input seismic motion of 10s..... | 24 |
| 1097 | Figure 6 : Stress-strain curve for a soil element of shear strength 65kPa subjected to the | |
| 1098 | first two cycles of a sinusoidal input seismic motion. | 24 |
| 1099 | Figure 7: Comparison of the acceleration at the surface of P1 profile, for the pulse-like | |
| 1100 | input motion, for the linear elastic computation and for the elastic substratum case. | |
| 1101 | | 28 |
| 1102 | Figure 8 Comparison of the acceleration at the surface of P1 profile, for the pulse-like | |
| 1103 | input motion, for the linear visco-elastic computation and for the rigid substratum | |
| 1104 | case..... | 28 |
| 1105 | Figure 9 : Comparison of the surface to reference Fourier spectra ratio, for the non- | |
| 1106 | linear comparison using for the left sub-graphs the high frequency input motion | |
| 1107 | and for the right sub-graphs the low-frequency input motion and with for the first | |
| 1108 | line the weakest input motion PGA and the second line the highest input motion | |
| 1109 | PGA..... | 31 |
| 1110 | Figure 10 : Comparison of the acceleration pseudo-response spectra at the ground | |
| 1111 | surface, for the non-linear computation using for the left sub-graphs the high | |
| 1112 | frequency input motion and for the right sub-graphs the low-frequency input | |
| 1113 | motion and with for the first line the weakest input motion PGA and the second line | |
| 1114 | the highest input motion PGA..... | 31 |
| 1115 | Figure 11 : Standard deviation (in log unit) of the transfer function (left panel) and | |
| 1116 | response spectra (right panel) depending of the input motion used..... | 31 |

1117 Figure 12 : Peak shear strain profiles reached at each depth by each team for the high
1118 and low frequency reference motion scaled at the highest PGA level (5 m/s²), for
1119 the profile 1 and for rigid substratum conditions.....31

1120 Figure 13 : Standard deviation (in log₁₀ unit) of the PGA at the surface of the P1 profile,
1121 for the 5 different computational cases (linear –elastic, linear visco-elastic, non-
1122 linear with input motion scaled to the lowest (0.5m/s²), medium (1m/s²) and
1123 highest (5m/s²) PGA, for the pulse-like, the high frequency and the low frequency
1124 content motions. The left sub-plot shows the results for the rigid substratum case
1125 and the right sub-plot for the elastic substratum..... 33

1126 Figure 14 : Standard deviation (in log unit) of the different intensity parameters for the
1127 P1 profile, for the 5 different computational cases (linear –elastic, linear visco-
1128 elastic, non-linear with input motion scaled to the lowest (0.5m/s²), medium
1129 (1m/s²) and highest (5m/s²) PGA, for the low frequency content motion. The left
1130 sub-graph shows the results for the rigid substratum case and the right sub-graph
1131 for the elastic substratum..... 34

1132 Figure 15 : Standard deviation (in log unit) of the PGA for the profile 1 2 and 3, for the 5
1133 different computational cases (linear –elastic, linear visco-elastic, non-linear with
1134 input motion scaled to the lowest (0.5m/s²), medium (1m/s²) and highest (5m/s²)
1135 PGA, for the low frequency content motion and for the rigid substratum case. 35

1136 Figure 16 : Stress-strain curves at the bottom of P1 Profile for the Rigid substratum case
1137 subjected to the low frequency motion (in color and the high frequency motion in
1138 black scaled to the highest PGA (5m/s²). The grey curves are for code/team couples
1139 that exceed the specified shear strength of 65 KPa, whereas the coloured curves

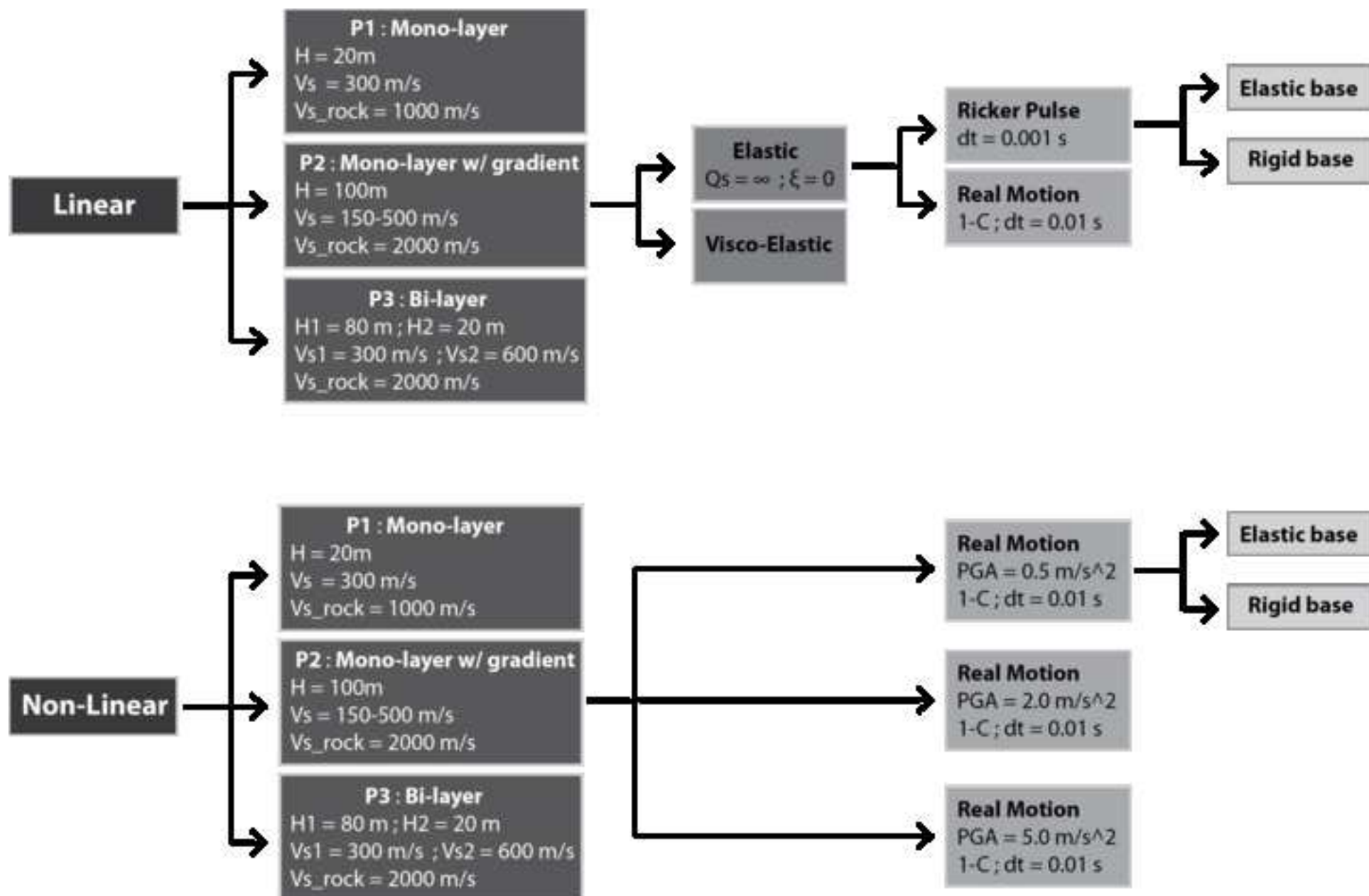
1140 represent the code/team couples that use 65 KPa. The red curves are for codes
1141 using damping control and the blue curves the others.....37

1142 Figure 17 : Standard deviation values (σ_{\log} , in \log_{10} units) of four parameters for the non-
1143 linear computation using the low-frequency content input motion scaled to the
1144 highest PGA : PGA (upper left), Response spectra at 0.27 s (upper right), Response
1145 spectra at 0.09 s (lower left) all three at the surface of P1 and the maximal shear
1146 deformation at the bottom of the P1 profile (lower right). The standard deviation
1147 are given for each group of the four groupings: depending on their low strain
1148 attenuation implementation (G-1) their numerical scheme (G-2) their constitutive
1149 models (G-3) and their values of shear strength at the bottom of P1 and use of
1150 damping control or not (G-5). The grey area illustrates the standard deviation for all
1151 code/team couples.....38

1152 Figure 18 : Comparison of the pseudo- acceleration response spectra at the ground
1153 surface of P1 with rigid substratum condition, for the non-linear computation using
1154 for the left sub-graphs the high frequency input motion and for the right sub-graphs
1155 the low-frequency input motion and with for the first line the middle input motion
1156 PGA and the second line the highest input motion PGA. The response spectra were
1157 sorted according to three groups: group 1 is composed of the code/team couples
1158 using similar τ_{\max} and damping control constitutive model. Group 2 use similar τ_{\max}
1159 and no damping control and Group 3 are the other code team couples.39

1160

1161



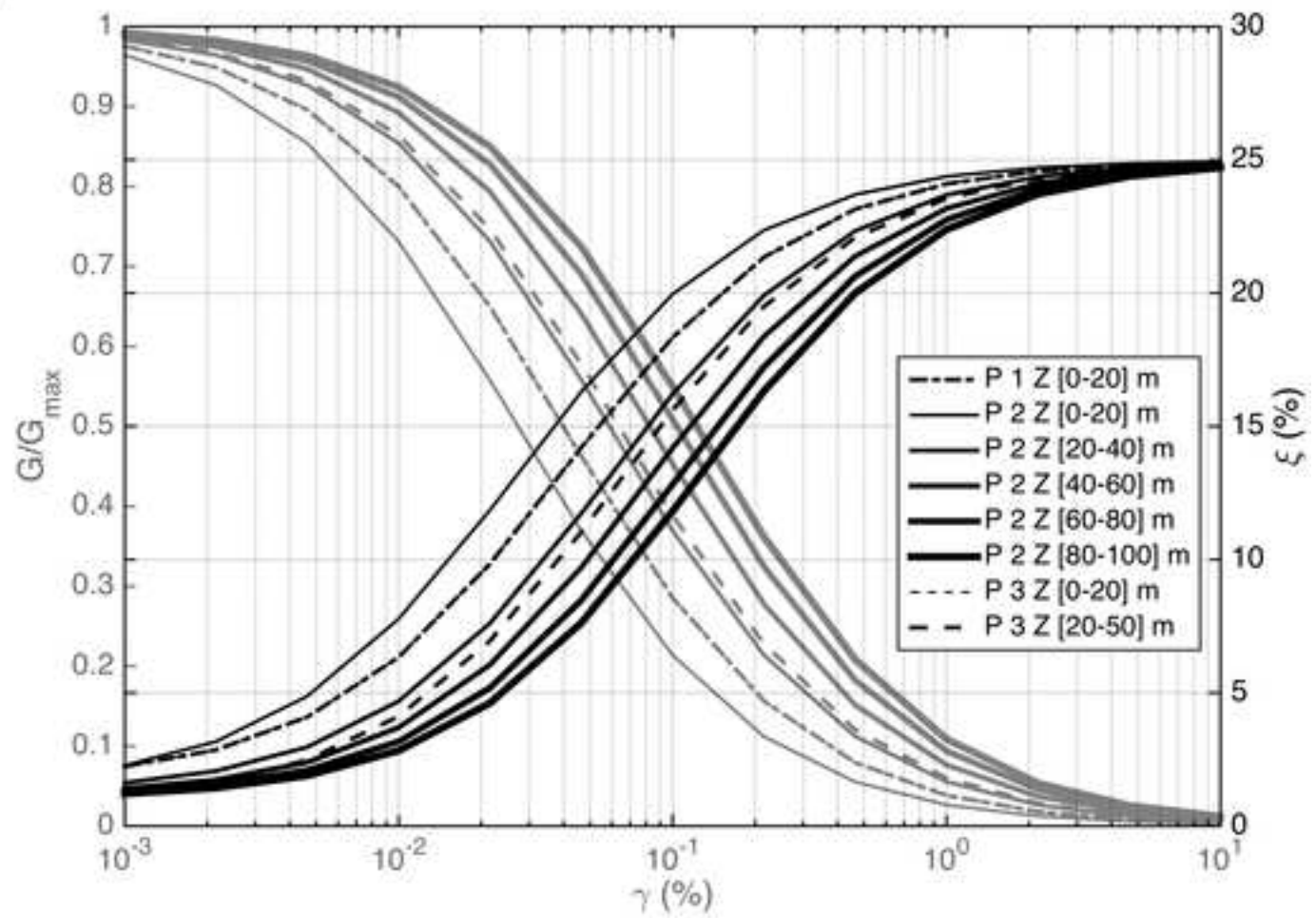
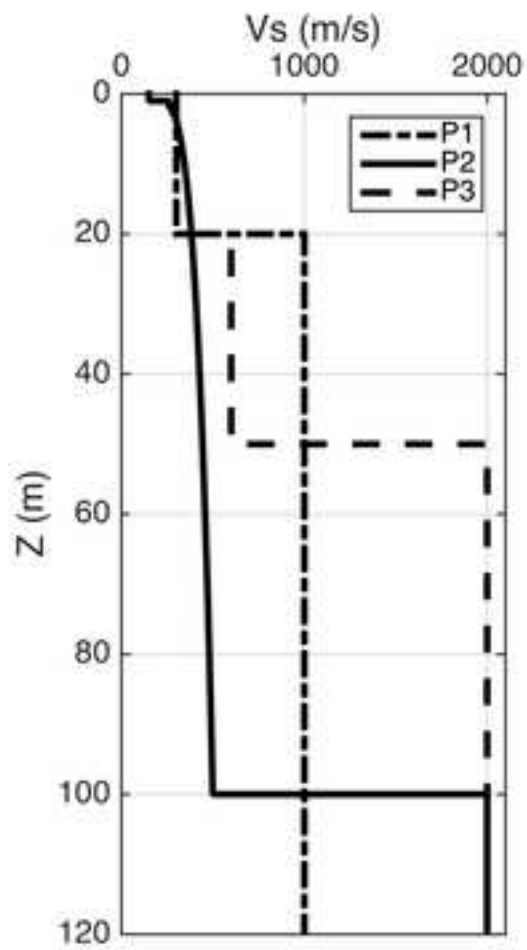


Figure 3

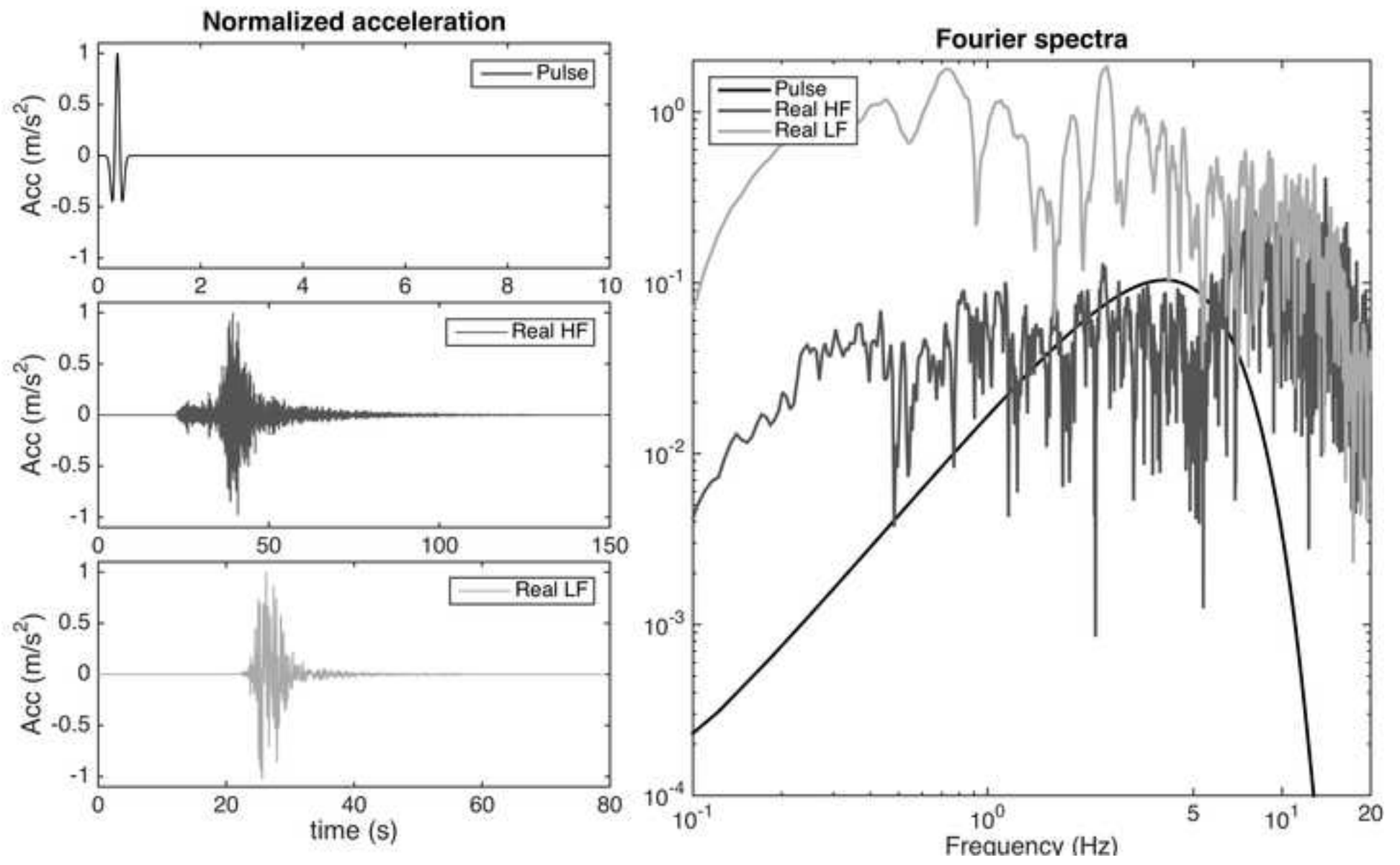


Figure 4

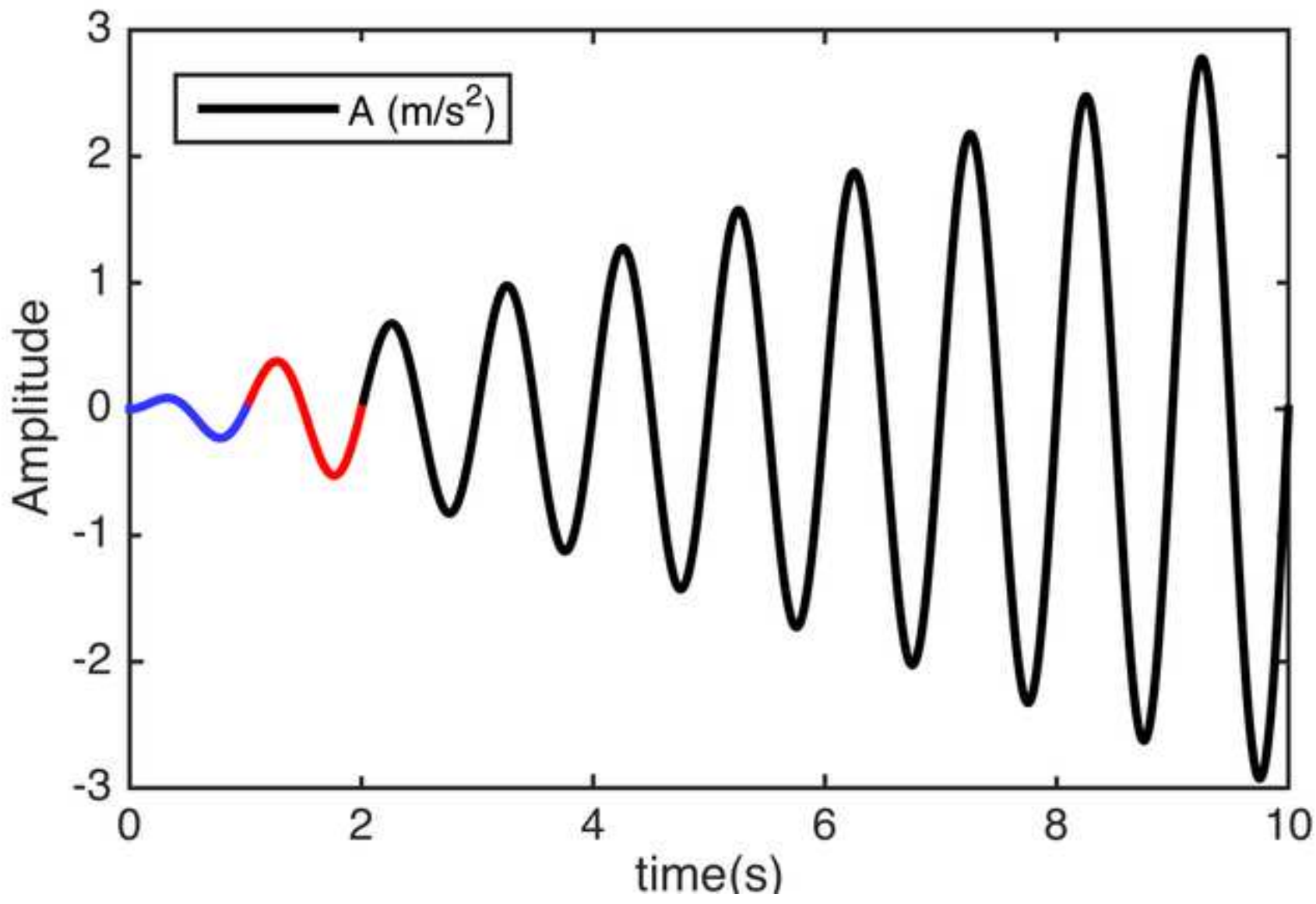


Figure 5

[Click here to download Figure fig_5_ss_temps_P1_NL_sinus_1_R_Z10_all.png](#)

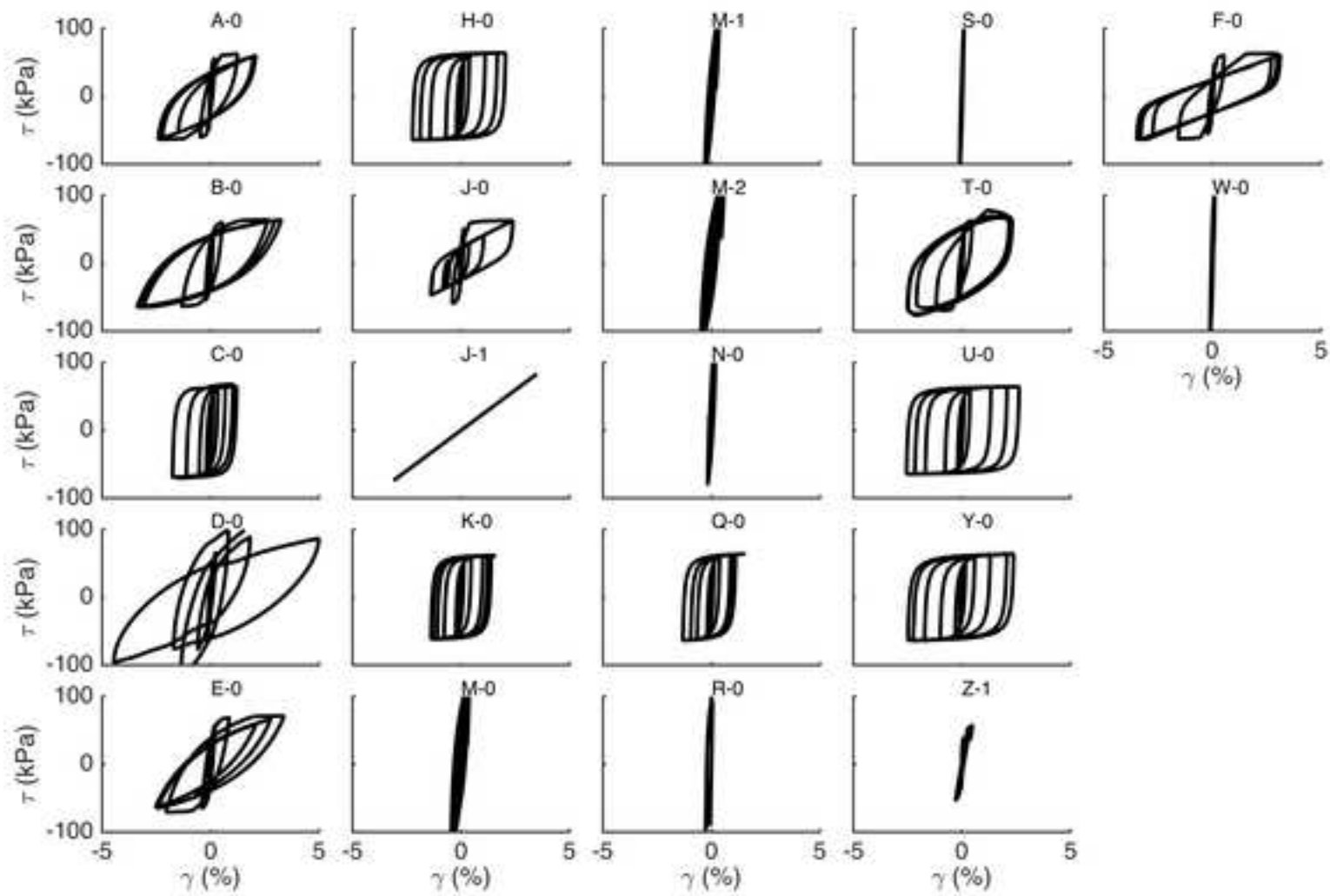
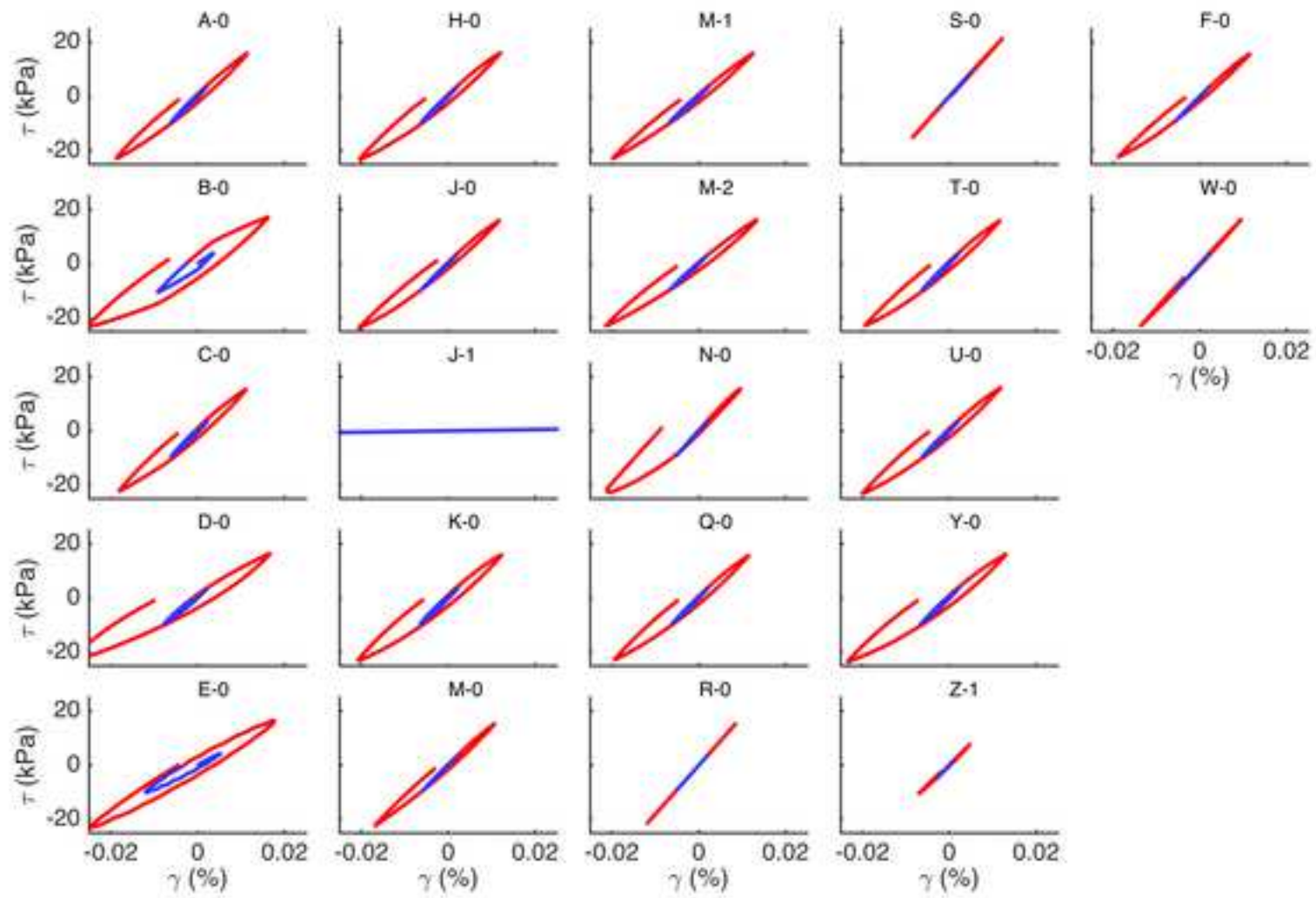


Figure 6

[Click here to download Figure fig_6_ss_temps_P1_NL_sinus_1_R_Z10_1_2_cycles_2.png](#)

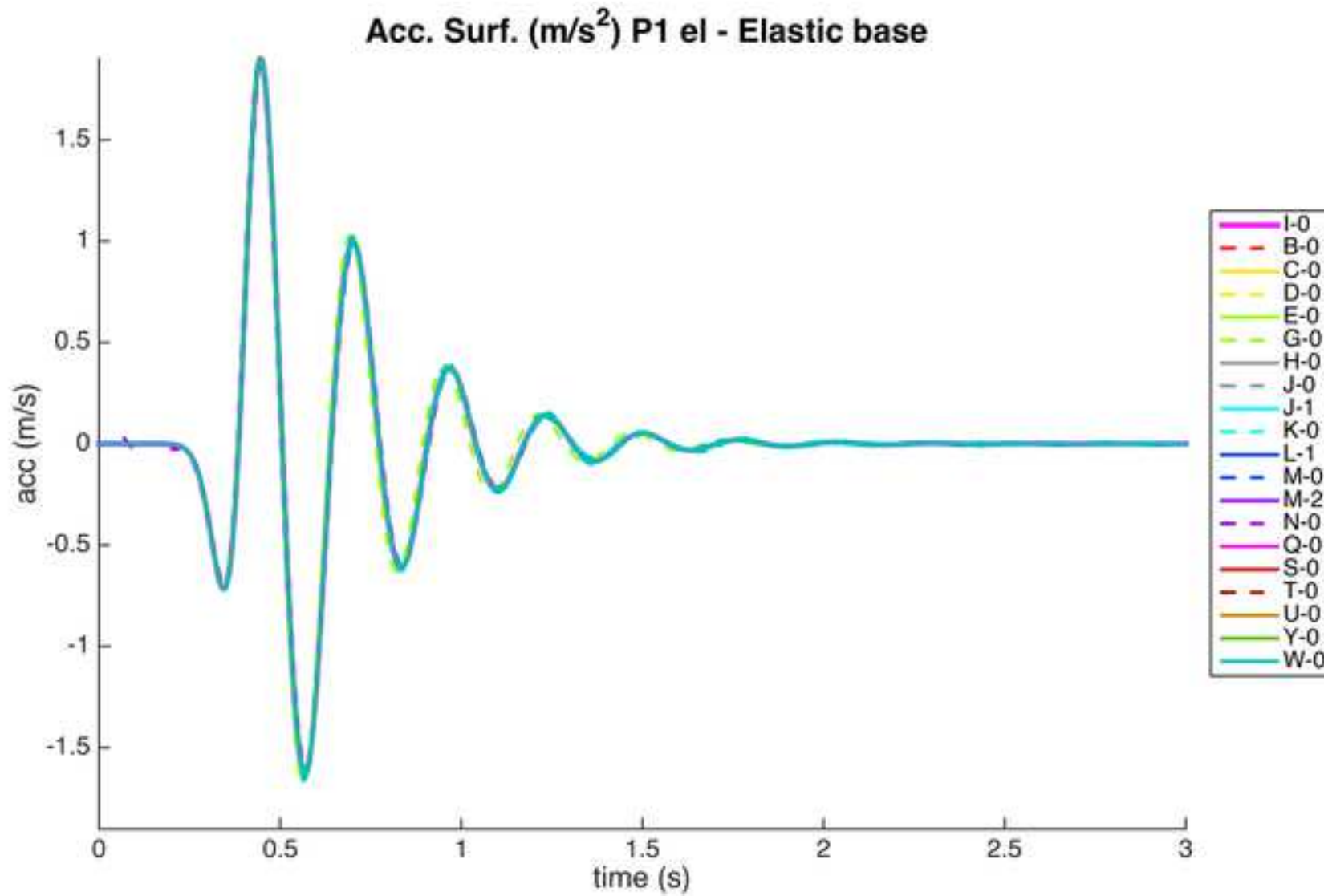


Figure 8

